JBC RESEARCH ARTICLE

Structural basis of human IL-18 sequestration by the decoy receptor IL-18 binding protein in inflammation and tumor immunity

Received for publication, February 14, 2022, and in revised form, April 3, 2022 Published, Papers in Press, April 6, 2022,
https://doi.org/10.1016/j.jbc.2022.101908

Sam Detry[1,2,‡], **Julie Andries**[1,2,‡], **Yehudi Bloch**[1,2], **Cem Gabay**[3], **Danielle M. Clancy**[1,2], and **Savvas N. Savvides**[1,2,*]

From the [1]*Unit for Structural Biology, Department of Biochemistry and Microbiology, Ghent University, Ghent, Belgium;* [2]*Unit for Structural Biology, VIB Center for Inflammation Research, Ghent, Belgium;* [3]*Division of Rheumatology, Department of Medicine, Geneva University Hospitals & Faculty of Medicine University of Geneva, Geneva 14, Switzerland*

Edited by Wolfgang Peti

Human Interleukin-18 (IL-18) is an omnipresent proinflammatory cytokine of the IL-1 family with central roles in autoimmune and inflammatory diseases and serves as a staple biomarker in the evaluation of inflammation in physiology and disease, including the inflammatory phase of COVID-19. The sequestration of IL-18 by its soluble decoy receptor IL-18-Binding Protein (IL-18BP) is critical to the regulation of IL-18 activity. Since an imbalance in expression and circulating levels of IL-18 is associated with disease, structural insights into how IL-18BP outcompetes binding of IL-18 by its cognate cell-surface receptors are highly desirable; however, the structure of human IL-18BP in complex with IL-18 has been elusive. Here, we elucidate the sequestration mechanism of human IL-18 mediated by IL-18BP based on the crystal structure of the IL-18:IL-18BP complex. These detailed structural snapshots reveal the interaction landscape leading to the ultra-high affinity of IL-18BP toward IL-18 and identify substantial differences with respect to previously characterized complexes of IL-18 with IL-18BP of viral origin. Furthermore, our structure captured a fortuitous higher-order assembly between IL-18 and IL-18BP coordinated by a disulfide-bond distal to the binding surface connecting IL-18 and IL-18BP molecules from different complexes, resulting in a novel tetramer with 2:2 stoichiometry. This tetrapartite assembly was found to restrain IL-18 activity more effectively than the canonical 1:1 complex. Collectively, our findings provide a framework for innovative, structure-driven therapeutic strategies and further functional interrogation of IL-18 in physiology and disease.

Originally discovered in mice as interferon-γ-inducing factor, Interleukin-18 (IL-18) was found to be a potent inducer of interferon-γ (IFN-γ) production in synergy with IL-12 upon exposure to intracellular pathogens (1–3). It was subsequently cloned and identified as an 18-kDa cytokine belonging to the IL-1 cytokine family and renamed to IL-18 (4). Similar to other IL-1 family cytokines, IL-18 is expressed as an inactive precursor protein that requires cleavage by caspase-1 for full biological activity (5, 6). While approximately 80% of pro-IL-18 is retained intracellularly, the rest is released by macrophages/monocytes and dendritic cells after maturation by caspase-1 (7, 8). Mature IL-18 initiates signaling by establishing a tripartite complex with IL-18 receptor alpha (IL-18Rα) and IL-18 receptor beta (IL-18Rβ), the latter also known as IL-18 receptor accessory protein and IL-1R7. The heterodimerization of the receptors' intracellular Toll/IL-1 receptor domains triggers recruitment of the adapter protein myeloid differentiation primary response 88 (MyD88), which further activates the downstream signaling cascade through IRAK-1/4, TRAF6, and NFκB (9–12). IL-18 is mainly involved in the activation of NK and T helper 1 cells and IFN-γ production in response to intracellular bacteria or viruses (13, 14).

Due to its highly proinflammatory and pleiotropic activity, IL-18 signaling is highly regulated at many levels to prevent uncontrolled inflammation. Akin to other IL-1 family cytokines, this regulation is achieved through gene regulation (15), caspase-1 activation (5, 6), and importantly, is also mediated by a soluble decoy receptor (16). Once IL-18 is activated and released from immune cells, its availability is mainly regulated by sequestration by IL-18-binding protein (IL-18BP), a dedicated soluble decoy receptor-like protein capable of blocking the biological activity of IL-18 (17). Even though IL-18BP functions as a decoy receptor, it is not homologous to any extracellular domain of the IL-18 receptors and is encoded as a separate gene (18), an oddity in the cytokine field (19). However, bioinformatic approaches have proposed that IL-18BP is evolutionary related to TIGIRR-1 (aka IL-1R9) and is thus regarded as a member of the IL-1 receptor family. In addition, sequence and functional homology lead to the identification of IL-18BP orthologs in all orthopox viruses (20, 21), including ectromelia poxvirus IL-18-binding protein (ectvIL-18BP) and yaba-like disease virus IL-18-binding protein (yldvIL-18BP) (22, 23), that act as virulence factors by attenuating immune responses mediated by IL-18.

Not only is human IL-18BP present in the serum at a 20-fold molar excess (24), it also has an exceptionally high affinity ($K_D \sim 300$ pM) for IL-18 (25), in contrast to IL-18Rα's

‡ These authors contributed equally to this work.
* For correspondence: Savvas N. Savvides, savvas.savvides@ugent.be.

affinity toward hIL-18, which is reported to be several orders of magnitude weaker ($K_D \sim 69$ nM) (26). Intriguingly, the affinity of viral IL-18BPs for human IL-18 is considerably lower than human IL-18BP ($K_D \sim 1$ nM), although they display picomolar affinity toward mouse IL-18 (25). As a result, IL-18 is sequestered by IL-18BP under homeostatic conditions, thereby preventing it from signaling through its receptors and evoking unwanted proinflammatory responses. Interestingly, IL-18-induced IFN-γ upregulates IL-18BP expression, creating a negative feedback loop to dampen and resolve inflammation (27, 28). Several (auto)immune diseases have been associated with increased levels of IL-18 such as rheumatoid arthritis (RA) (29, 30), Crohn's disease (CD) (31, 32), and systemic lupus erythematosus (33–35). As IL-18BP has a high IL-18 sequestration capacity (35), the balance between IL-18/IL-18BP and the concentrations of free IL-18, instead of total IL-18, are more relevant to measure to evaluate inflammatory responses (36). Elevated levels of free IL-18 have been identified in hyperinflammatory diseases such as macrophage activation syndrome and systemic juvenile idiopathic arthritis (28, 37). Furthermore, in mouse models of macrophage activation syndrome, IL-18BP-deficient mice developed more severe disease manifestations, pointing to the crucial role of IL-18BP activity in this setting (28). In addition, elevated levels of IL-18 in blood and bronchoalveolar lavage fluid from coronavirus patients have been shown to correlate with COVID-19 disease severity and worse clinical outcomes (38–40).

Unsurprisingly, IL-18-neutralizing antibodies or recombinant IL-18BP have been successfully used to mitigate IL-18 related pathologies (41, 42). Clinical trials using recombinant hIL-18BP (Tadekinig α) for adult-onset Still's disease (AOSD), RA, and plaque psoriasis show promising safety and indicative signs of efficacy in patients with AOSD (43, 44). On the other hand, administration of recombinant IL-18 in mouse tumor models was shown to elicit favorable antitumoral effects in synergy with chimeric antigen receptor T and immune checkpoint inhibitors (45). Whereas such findings provided a strong rationale for the therapeutic potential of IL-18 in cancer (46), its efficacy has not lived up to expectations (47), the culprit being the concomitant increase in the serum concentration of IL-18BP by up to 100-fold in patients (46, 48).

To aid further advancements in the mechanistic interrogation of IL-18 sequestration by IL-18BP and the therapeutic targeting of hIL-18 and hIL-18BP in infectious diseases, inflammation, and cancer, structural details of their complex and of interaction interface to high resolution would be opportune. Here, we present the crystal structure of human IL-18 in complex with human IL-18BP. This study shows that hIL-18BP binds hIL-18 at the same epitope as IL-18Rα and viral IL-18BPs using a large hydrophobic patch flanked by two tightly fitting hydrophobic pockets complemented by salt bridges. A crucial advance in our crystallization efforts was the elimination of the flexible N-terminus and minimization of heterogenous glycosylation patterns of hIL-18BP while retaining functional and biological activity. Moreover, we discovered a novel disulfide-linked interface resulting in an unexpected tetrameric assembly of hIL-18 and hIL-18BP. The structural model presented here is imperative to validate previous models, map key differences between human and viral orthologs of IL-18BP, and allows advancements in the design of novel inhibitors or antagonists.

Results

Human IL-18BP can be truncated to a bioactive core structure with reduced glycosylation

To enable structural studies of the human IL-18BP:IL-18 complex by X-ray crystallography, we initially considered clinical grade human IL-18BP (Tadekinig alfa) that was used in a phase 2 clinical trial to evaluate the safety and efficacy of IL-18BP in AOSD (43). However, due to the extensive glycosylation of this protein and the need to create glycan-engineered protein amenable to structural studies by X-ray crystallography, we produced full-length hIL-18BP in transiently transfected HEK293S MGAT1$^{-/-}$ cells allowing for N-linked glycosylation as $Man_5GlcNAc_2$ glycans (49) and mature hIL-18 in *Escherichia coli*. Using size-exclusion chromatography (SEC) and in-line multi-angle laser light scattering (MALLS), we found that full-length hIL-18BP was heavily glycosylated with nearly 50% of its mass accounted for by glycans (Fig. 1*A* and Table 1), consistent with predictions (Fig. 2*A*). Furthermore, the distribution of mass across the SEC-MALLS peak for full-length hIL-18BP, the diffuse electrophoretic mobility of the purified protein in SDS-PAGE (Fig. 1, *A* and *B*), and large shifts in mass upon treatment with endoglucanases and O-glycosidases suggested heterogeneous glycosylation. Based on our experience with producing secreted glycoproteins with N-linked glycosylation and similar protein families in the HEK293T and HEK293S MGAT1$^{-/-}$ cell lines for structural biology (50–53), we reasoned that this most likely originates from O-glycans and possible differences in N- and O-glycosylation site occupancy. Initial crystallization trials using purified hIL-18BP$_{FL}$:IL-18 complex containing glycan-shaved hIL-18BP$_{FL}$ and displaying apparent stoichiometry of 1:1 as evaluated by SEC-MALLS did not lead to candidate crystallization conditions even when employing hIL-18BP$_{FL}$:IL-18 complex up to 30 mg/ml. Such apparent high solubility during crystallization trials was deemed to be consistent with the observed extensive and heterogeneous glycosylation of hIL-18BP$_{FL}$ (Fig. 1*A* and Table 1). Therefore, we sought to produce alternative versions of hIL-18BP that would be more amenable to structural studies. Sequence alignment of hIL-18BP with homologous viral IL-18BPs, for which structural information is available (22, 23), suggested that the expected core beta-sandwich domain of hIL-18BP (residues 63–171) might be flanked by N- and C-terminal stretches (residues 31–62 and 170–194, respectively) bearing intrinsic disorder and the majority of the predicted O-glycosylation sites (Fig. 2, *A* and *B*).

To this end, we produced hIL-18BP lacking the N- and/or C-terminal regions in HEK293S MGAT1$^{-/-}$ cells. We found that only hIL-18BP truncated at the N-terminus (residues 63–194), hereafter termed hIL-18BP$_{ΔN}$, could be sufficiently

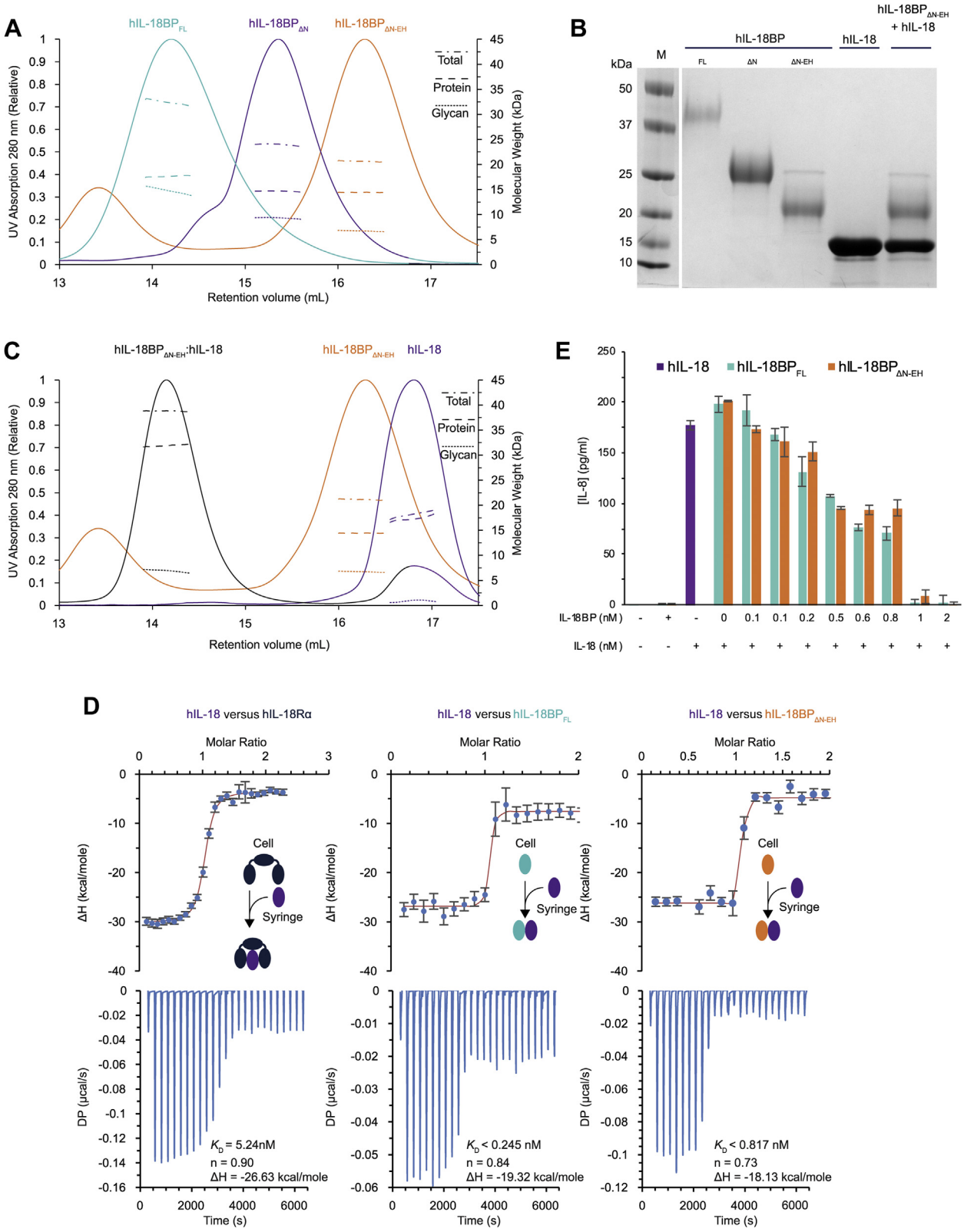

Figure 1. Biochemical characterization and functional activity of human IL-18 and IL-18BP. *A*, SEC-MALLS analysis of hIL-18BP$_{FL}$, hIL-18BP$_{\Delta N}$, and hIL-18BP$_{\Delta N\text{-}EH}$ protein (complex), respectively, yielding less glycosylated and more homogenous material for crystallization purposes. *B*, SDS-PAGE of hIL-18BP$_{FL}$, hIL-18$_{\Delta N}$, and hIL-18BP$_{\Delta N\text{-}EH}$ show decline in total protein and glycan mass caused by removal of O-glycosylated N-terminus and shaving of N-glycans by Endoglycosidase H (EH). SDS-PAGE of hIL-18 and hIL-18:hIL-18BP$_{\Delta N\text{-}EH}$ complex show presence and purity of both proteins. *C*, SEC-MALLS analysis of hIL-18:hIL-18BP$_{\Delta N\text{-}EH}$ complex prior to crystallization allow accurate stoichiometry determination (*A*) and (*C*) full lines show the SEC retention profile of samples (∼0.5–1 mg/ml) detected by UV (*left axis*, 280 nm). Interrupted lines show the molecular weights in kDa of the sample over the course of the SEC peak, split up by protein conjugate analysis in total (*dashed* and *dotted*), protein (*dashed*), and glycan (*dotted*) mass (*right axis*). *D*, isothermal titration calorimetry (ITC) of hIL-18 in hIL-18Rα, hIL-18BP$_{FL}$, and hIL-18BP$_{\Delta N\text{-}EH}$, which shows recombinantly produced hIL-18 and hIL-18BP$_{\Delta N\text{-}EH}$ are both functionally competent.

Table 1
Molecular weights of recombinant proteins used in this study and IL-18:receptor complexes as estimated *via* SEC-MALLS and binding parameters for the binding of hIL-18 to receptors as determined by ITC

		Molecular weight determined by MALLS			Binding to hIL-18 determined by ITC	
Protein (complex)	MW (kDa)	Total MW ± SD (kDa)	Protein MW ± SD (kDa)	glycan MW ± SD (kDa)	K_D (95% CI) (nM)	ΔH (95% CI) (kcal/mole)
hIL-18	18.2	18.2 ± 0.5	–	–	–	–
hIL-18BP$_{FL}$	17.6	32.4 ± 0.5	17.6 ± 0.1	14.8 ± 0.6	n.d. (−∞ to 0.245)	−19.32 (−18.33 to −20.32)
hIL-18BP$_{\Delta N}$	14.4	24.0 ± 0.2	14.65 ± 0.06	9.3 ± 0.1	–	–
hIL-18BP$_{\Delta N\text{-}EH}$	14.4	21.12 ± 0.09	14.42 ± 0.02	6.71 ± 0.08	n.d. (−∞ to 0.817)	−18.13 (−16.91 to −19.36)
hIL-18hIL-18BP$_{\Delta N\text{-}EH}$	32.6	38.80 ± 0.06	31.9 ± 0.2	6.9 ± 0.2	–	–
hIL-18Rα	35.4	–	–	–	5.24 (7.94 to 3.38)	−26.63 (−25.59 to −27.77)

Abbreviations: MW, Molecular weight; CI, Confidence interval; MALLS, Multi-Angle Laser Light Scattering; ITC, Isothermal Titration Calorimetry.

produced for structural studies. SEC-MALLS analysis of hIL-18BP$_{\Delta N}$ revealed the loss of 3 kDa of protein mass and 5.5 kDa of glycans (Fig. 1*A* and Table 1), confirming that the N-terminus of hIL-18BP is heavily glycosylated. Additional trimming of N-linked $Man_5GlcNAc_2$ glycans using Endoglycosidase H (Endo H) resulted in a further loss of 2.5 kDa of N-linked glycans (Fig. 1, *A* and *B*).

We initially verified the functional activity of hIL-18BP$_{\Delta N}$ treated with Endo H (IL-18BP$_{\Delta N\text{-}EH}$) in terms of its ability to sequester hIL-18 in stoichiometric fashion and high affinity. Indeed, SEC-MALLS analysis showed that hIL-18BP$_{\Delta N\text{-}EH}$ can establish a monodisperse complex with hIL-18 according to a 1:1 stoichiometry (Fig. 1*C* and Table 1). Using isothermal titration calorimetry, we compared the thermodynamic binding profiles and affinities of hIL-18BP$_{FL}$, hIL-18BP$_{\Delta N\text{-}EH}$, and the hIL-18 cognate receptor (IL-18Rα) to hIL-18 (Fig. 1*D*). Our data show that hIL-18BP$_{\Delta N\text{-}EH}$ and hIL-18BP$_{FL}$ are virtually indistinguishable from each other in their thermodynamic binding profiles and sub-nM affinities toward hIL-18. In contrast and consistent with previously published data (26), human hIL-18Rα binds to hIL-18 with lower affinity (K_D = 4.7 nM) than hIL-18BP. However, the binary complex affinity measured here is markedly higher than previously reported affinities (K_D∼60 nM) (26) by surface plasmon resonance.

Finally, we interrogated the biological activity of hIL-18BP$_{\Delta N\text{-}EH}$ by using the hIL-18-responsive macrophage cell line KG-1, the activity of which is manifested by NFκB signaling and proinflammatory cytokine and chemokine production (54). In this context, we measured the amount of IL-8 secreted from KG-1 cells upon hIL-18 stimulation and found that both hIL-18BP$_{FL}$ and hIL-18BP$_{\Delta N\text{-}EH}$ display comparable inhibitory activities. (Fig. 1*E*).

Structural mimicry underlies the sequestration of human IL-18 by IL-18BP

Structural insights into the sequestration of human IL-18 by its cognate decoy receptor IL-18BP had remained elusive despite the growing importance of IL-18BP in physiology and disease. Using the truncated and glycan-shaved hIL-18BP$_{\Delta N\text{-}EH}$, we purified crystallization-grade hIL-18:hIL-18BP$_{\Delta N\text{-}EH}$ complex and determined the crystal structure of the complex to 1.8 Å resolution by molecular replacement using the crystal structure of ectvIL-18BP (23) (pdb 3f62) as a search model (Fig. 3*A* and Table 2). Crystallographic refinement and the quality of the ensuing electron density maps were enhanced after correcting the X-ray data for data anisotropy using the STARANISO server (55). The crystal asymmetric unit contains one copy of the 1:1 complex and reveals how hIL-18BP uses the side of its h-type immunoglobulin β-sandwich fold to bind the β-trefoil structure hIL-18 (Fig. 3*A*). hIL-18BP harbors two internal disulfide bridges connecting strands A and B (Cys86-Cys150), and B and F (Cys64-Cys89). In addition, three predicted N-glycan sites are occupied by GlcNAc at residues Asn79, Asn103, and Asn147. Our model for hIL-18BP starts at the beginning of the hIL-18BP$_{\Delta N}$ construct, that is, Gln63, however no density was observed past Ala170 in the crystal solvent channels, consistent with the predicted disorder of the C-terminal tail (Figs. 3*C* and 2*B*). Human IL-18 features its signature β-trefoil fold and closely resembles the structure of unbound hIL-18 (pdb 3wo2) (all-atom r.m.sd=1.8 Å). Structure-based sequence alignments of human IL-18BP and structural superpositions against the two structurally characterized viral IL-18BPs, ectvIL-18BP and yldvIL-18BP, and domain 3 of hIL-18Rα (hIL-18Rα$_{D3}$) establish the strong conservation of the adopted fold, albeit with major variations in the CD loop mediating hIL-18 binding and AB loop (Fig. 3, *B*–*D*). Importantly, these analyses reveal that structural mimicry and direct steric competition underlie the sequestration of human hIL-18 by hIL-18BP (Fig. 3*C*).

Specifically, human IL-18BP covers the top of the hIL-18 β-barrel with one side of its β-sandwich scaffold composed of strands C, G, and F and is slightly inclined to enable protrusion of loops FG and BC into the barrel. Additionally, residues from the CD loop and D strand mediate important interactions on the other side of the sheet (Fig. 3*A*). Considering the plethora of structural information on human/viral IL-18BPs and human IL-18Rα in complex with hIL-18,

Bottom plots show the raw baseline-subtracted thermograms while *top* plots show integrated heats (*blue dots*) with fitted isotherm (*red line*). Diagrams in the isotherm plot show which protein was in the cell or syringe and what the expected final complex looks like. *E*, bar plot of IL-8 levels in conditioned media after hIL-18 stimulation in presence or absence of hIL-18BP$_{FL}$ or IL-18BP$_{\Delta N\text{-}EH}$. Recombinant IL-18 was preincubated for 1 h at 37 °C with the indicated concentrations of full-length IL-18BP or IL-18BP$_{\Delta N\text{-}EH}$. KG-1 cells were left untreated (UT) or stimulated with IL-18 (*purple*) (0.5 nM final concentration) ± IL-18BP (*teal* and *orange*), as indicated. After 18 h, IL-8 concentration in cell culture supernatants was measured by ELISA. Error bars display standard deviation (SEM). IL-18, interleukin-18; SEC, size-exclusion chromatography; MALLS, multi-angle laser light scattering.

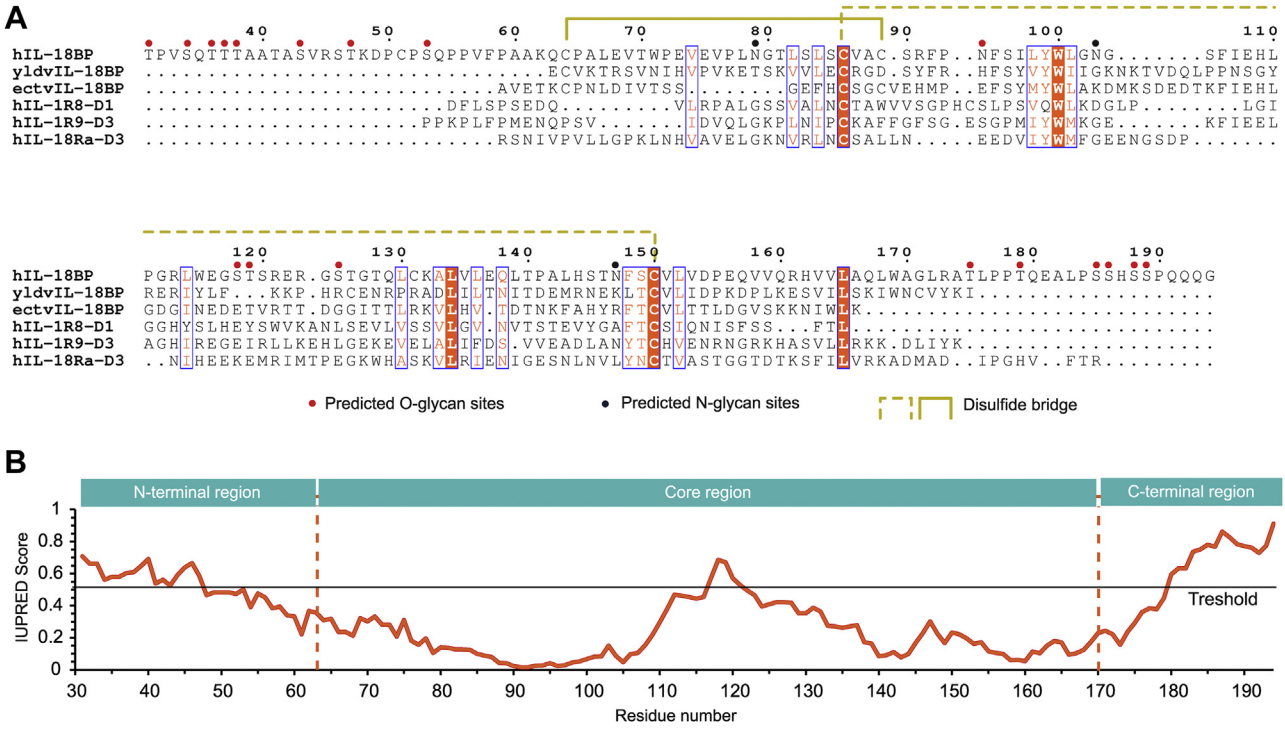

Figure 2. Protein sequence analyses of human IL-18BP. *A*, sequence alignment performed by Clustal Omega (71) visualized by ESPript (76) of hIL-18BP and related sequences. The core-region was delineated based on the sequence alignment, disordered region prediction, and existing crystal structures of viral IL-18BPs. Gaps in the sequence alignment are represented by *dots*. Residues with strict identity have an *orange* background, and residues with similarity are colored *orange*. Groups of high similarity residues are surrounded by a *blue box*. Predicted N- (73) and O-glycan (74) sites are displayed as *blue* and *red dots*, respectively. Cysteine disulfides are represented by *yellow lines* (*full* or *dashed*). *B*, IUPRED prediction (75) of disordered regions in human IL-18BP shows that the extended N- and C-termini are likely disordered and flexible. Disorder threshold is represented by a *black horizontal line*. Delineation of tested terminal truncations is represented by *vertical dashed orange lines*.

curation and comparison of the observed interaction interfaces to distil key structure-function insights presents with considerable challenges. At the same time, annotation of amino acid positions that have been interrogated by mutagenesis would also be desirable. Together, such analyses could lead to a rationale for the exquisitely efficient sequestration of hIL-18 by hIL-18BP and might further fuel protein engineering approaches to modulate this sequestration potential. Therefore, we sought to develop a representation scheme that would allow effective parallel comparison of all structural data available together with mutagenesis data (Fig. 4*B*). The binding interface can be subdivided into three sites: site A consists of complementary hydrophobic patches on both hIL-18 and hIL-18BP. Sites B and C each engage a phenylalanine on hIL-18BP, Phe106, and Phe95, respectively, to protrude into a hydrophobic cavity on hIL-18 sealed by salt bridges and hydrogen-binding interactions (Fig. 4*A*). Sequence alignments of hIL-18BP orthologs among vertebrates (Fig. 5*A*) allow mapping of highly conserved residues on the surface of hIL-18BP that mediate sequestration of hIL-18 and shows that this region of hIL-18BP is the most conserved compared to any other part of the decoy receptor (Fig. 5*B*). This suggests that the observed human IL-18BP:IL-18 complex can serve as a structural representative for all such complexes across species. When comparing the interface of human IL-18BP with its viral counterparts, these phenylalanine residues are largely conserved, except for yldvIL-18BP, which contains a threonine instead of phenylalanine at site B. The most striking difference is the lack of salt bridges in viral IL-18BPs at site C. Conversely, human IL-18Rα does form these salt bridges but lacks the phenylalanine residues protruding into the hydrophobic cavity of hIL-18, while also lacking another hydrophobic substitute. At site B, hIL-18Rα also lacks the phenylalanine residue but substitutes it for a methionine to fill the hydrophobic pocket (Fig. 4*B*). The absence of these phenylalanine residues in site B and C may explain the higher affinity of human IL-18BP to IL-18 than its receptor. Overall, site A is very similar for all interfaces with mainly conservative substitutions of key interacting residues. However, like IL-18Rα, but in contrast to the viral IL-18BPs, human IL-18BP exploits additional interactions *via* two side-chain-to-main-chain hydrogen bonds at site A.

A disulfide-linked interaction site mediates a novel higher-order IL-18:IL-18BP complex

An intriguing feature of the IL-18:IL-18BP complex concerns an unexpected disulfide bridge between Cys74 of hIL-18 in the canonical IL-18:IL-18BP complex and Cys131 of IL-18BP participating in a symmetry-related complex. This results in a covalent tetrameric assembly with a 2:2 stoichiometry and two-fold symmetry (Fig. 6*A*). We note that such higher-order assembly was not observed in the preparatory stages of precrystallization samples as assessed by SEC-MALLS or SDS-PAGE (Fig. 1, *B* and *C*). However, the sample was concentrated to 30 mg/ml prior to crystallization. To

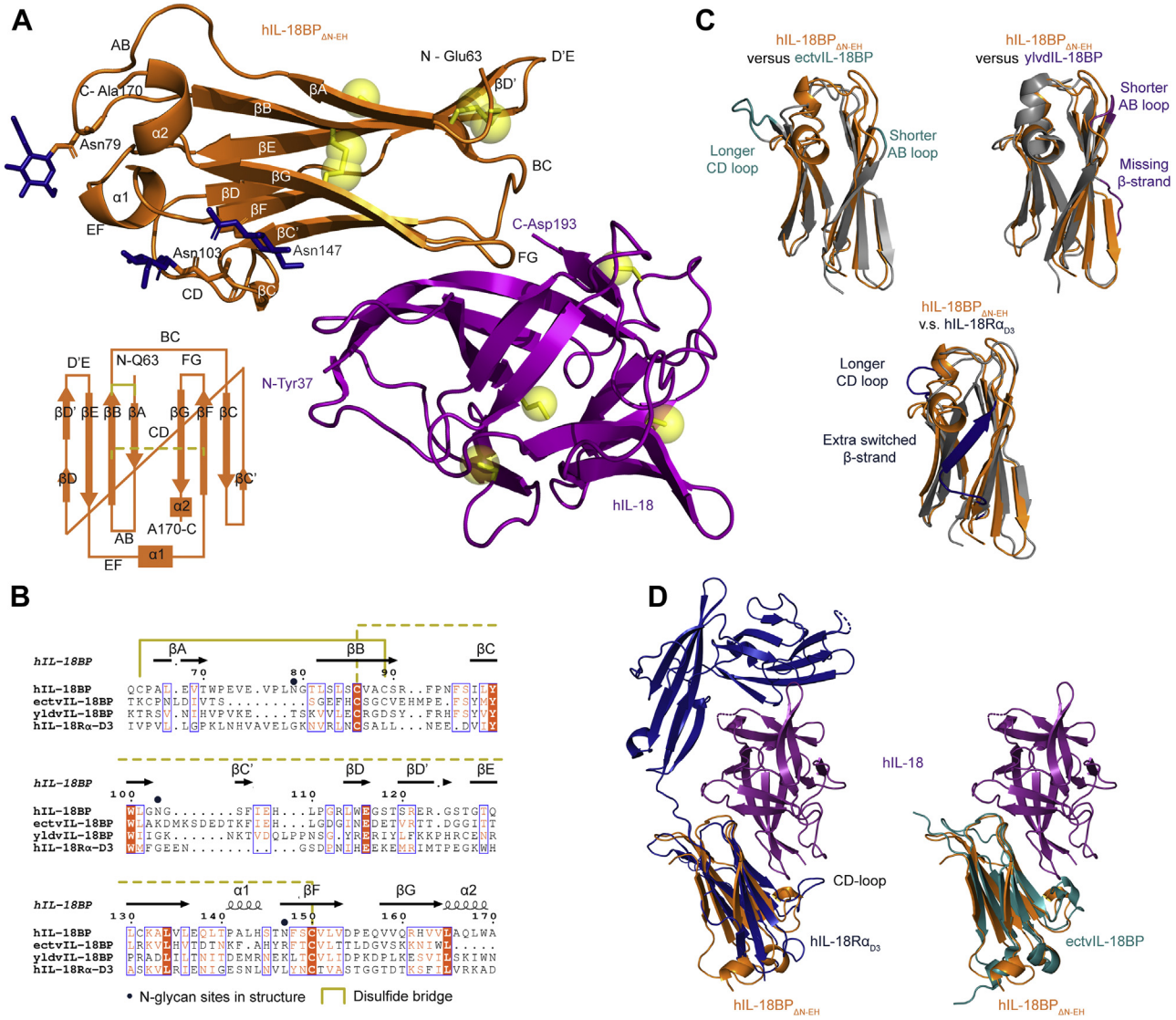

Figure 3. Crystal structure of the human IL-18:IL18BP complex and comparisons with human IL-18 receptor and viral decoy receptors. *A*, cartoon representation of asymmetric unit of the crystal structure of hIL-18:hIL-18BP$_{\Delta N\text{-}EH}$ displaying hIL-18 (*purple*) interacting with hIL-18BP$_{\Delta N\text{-}EH}$ (*orange*). Asparagine residues occupied with GlcNAc (*stick*, *blue*) are shown in *stick* representation as well as all cysteines (*yellow*). Secondary structures of hIL-18BP$_{\Delta N\text{-}EH}$, β-strands, α-helices, and loops are labeled in order of occurrence. Additionally, a schematic of the Ig-fold of hIL-18BP$_{\Delta N\text{-}EH}$ is shown in the *bottom left* in which cysteine bridges are represented by *yellow lines*. *B*, structural sequence alignment based on existing crystal structures performed in Swiss-PdbViewer (72) and visualized by ESPript (76) shows which residues spatially correspond to each other in the orthologous structures. Secondary structures are annotated by arrows (β-strand) and coils (α-helices) above the sequence. Linked disulfides are bridges by *yellow lines* (*full* or *dashed*). Asparagine residues occupied with GlcNAc in the model are labeled with *blue dots*. Residues with strict identity have an *orange* background and residues with similarity are colored *orange*. Groups of high similarity residues are surrounded by a *blue box*. *C*, crystal structure overlay of hIL-18BP$_{\Delta N\text{-}EH}$ (*orange*, pdb 7al7), ectvIL-18BP (*teal*, pdb 3f62 (22)), yldvIL-18BP (*purple*, pdb 4eee (23)), and hIL-18Rα (*dark blue*, pdb 3WO4 (26)) aligned to hIL-18BP$_{\Delta N\text{-}EH}$. Only notable differences on the level of secondary structures are colored accordingly, while stretches that align to hIL-18BP$_{\Delta N\text{-}EH}$ are left *gray*. Structural alignment of these structures shows that the core h-type Ig-fold is maintained with some strand and loop alterations, with an average all atom RMSD of 2.5 Å. Compared to human IL-18BP, ectv- and yldvIL-18BP have a shorter AB loop, while ectvIL-18BP has a significantly longer CD loop. *D*, cartoon representation of crystal structures of hIL-18BP$_{\Delta N\text{-}EH}$ (*orange*, pdb 7al7), ectvIL-18BP (*teal*, pdb 3f62 (22)), yldvIL-18BP (*purple*, pdb 4eee (23)), and hIL-18Rα (*dark blue*, pdb 3WO4 (26)) aligned to hIL-18 (*purple*, pdb 7al7). IL-18, interleukin-18; CD, Crohn's disease; ectvIL-18BP, ectromelia poxvirus IL-18-binding protein; yldvIL-18BP, yaba-like disease virus disease IL-18-binding protein.

verify whether such a higher-order complex originated during this final protein concentration step, the concentrated sample was diluted back to 0.5 mg/ml and analyzed by SDS-PAGE and SEC-MALLS. SDS-PAGE shows a band at ∼38 kDa which can be resolved to the constituent protein components upon the addition of the reducing agent DTT prior to loading the sample, indicating the presence of a disulfide linked dimer (Fig. 6*B*). We confirmed by mass spectrometry that both hIL-18 and hIL-18BP were present in this disulfide linked protein adduct, verifying a heterodimer as opposed to a homodimer of either. Additionally, SEC-MALLS shows that more than 90% of the previously concentrated sample now exists as a tetramer of 74 kDa, rather than the expected canonical IL-18:IL-18BP complex of 37 kDa (Fig. 6*C*). Protein conjugate analysis of SEC-MALLS data validated the presence of both hIL-18BP and hIL-18 in the complex with a 2:2

Table 2
Crystallographic data collection and refinement statistics

	Human IL-18:hIL-18BP$_{\Delta N\ EH}$	Human IL-18:hIL-18BP$_{\Delta N\ EH}$ corrected for diffraction-anisotropy
Data collection		
Wavelength (Å)	0.9762	0.9762
Resolution range (Å)	59.39–1.80 (1.87–1.80)	59.39–1.80 (1.85–1.80)
Space group	C 1 2 1	C 1 2 1
Unit cell (a, b, c (Å), α, β, γ (°))	109.82 44.52 60.28 90 99.86 90	109.82 44.52 60.28 90 99.86 90
Total reflections	183,218 (17,814)	140,440 (6871)
Unique reflections	26,507 (2546)	20,705 (1035)
Multiplicity	6.9 (7.0)	6.8 (6.6)
Completeness (%)	98.27 (96.15)	77.2 (49.6)
Mean I/σ(I)	15.67 (1.49)	18 (2.9)
Wilson B-factor (Å^2)	36.35	n.a.
R-meas	0.053 (1.327)	0.048 (0.680)
R-pim	0.020 (0.495)	0.018 (0.258)
CC1/2	0.999 (0.896)	0.999 (0.898)
CC*	1.000 (0.972)	n.a.
Refinement (59.39–1.8 Å)		
Reflections used in refinement	26,368 (2525)	20,691 (1306)
Reflections used for R-free	2640 (248)	2062 (130)
R-work/R-free[a]	0.207 (0.531)/0.230 (0.586)	0.188 (0.264)/0.217 (0.320)
CC (work)/CC (free)	0.968 (0.860)/0.959 (0.812)	0.874 (0.689)/0.858 (0.640)
Number of nonhydrogen atoms	2309	2309
Macromolecules	2136	2136
Ligands	42	42
Solvent	131	131
RMS bonds (Å)/angles (°)	0.011/1.34	0.011/1.34
Ramachandran favored (%)	98.05	98.05
Ramachandran allowed (%)	1.95	1.95
Ramachandran outliers (%)	0	0
Rotamer outliers (%)	0	0
Clash score	3.48	3.48
Average B-factor (Å^2)	34.68	34.68
Macromolecules	34.03	34.03
Ligands	66.67	66.67
Solvent	35.15	35.15

Values in parentheses correspond to the highest resolution shell (1.87–1.80 Å).
[a] 10% of reflections in R-free set.

stoichiometry, as any other combination of proteins and their glycans would not be compatible with their respective molecular masses.

Interestingly, in the structure of unbound hIL-18 and when in complex with its decoy and signaling receptors, the cysteine involved in the observed novel disulfide bond with IL-18BP is part of a 3_{10} helix and is not surface exposed (Fig. 6*A*, left panel). This region in inbound IL-18 is rather amphipathic in terms of physicochemical properties and interacts with several detergent molecules (CHAPS) in pdb 3wo2 (26). Thus, to participate in the observed disulfide bond, the cysteine has flipped outward and is accompanied by a structural rearrangement thereby disrupting the helical structure (Fig. 6*A*, left panel). Interestingly, an ensemble of structural models of IL-18 determined by NMR has shown this helix to be very flexible (56), which would favor such dynamics. We note that for the reported crystals structure of hIL-18 complexed with ectvIL-18BP and yldvIL-18BP (pdb 3f62 and 4eee respectively), all free cysteines were mutated to serine, thereby excluding the possibility of such a disulfide linkage, although this helix/loop segment was not modeled due to its apparent flexibility. Surrounding the cysteine disulfide bridge is a novel interface mediated by the beta strands E, B, D, and D′ of the opposite side of the beta-sandwich compared to the canonical interface and is maintained by a several hydrophobic residues on both molecules.

Because this hetero-tetramer was only initially observed with IL-18BP$_{\Delta N\text{-}EH}$ lacking the N-terminal and N-glycans, we also investigated if a similar higher-order complex could be formed with IL-18BP$_{FL}$ or endogenously glycosylated IL-18BP$_{\Delta N}$. Full-length IL-18BP was complexed with IL-18, concentrated to 0.5 mg/ml and analyzed by SEC-MALLS. No tetrameric complex was observed using IL-18BP$_{FL}$, either in its glycosylated or deglycosylated form, suggesting that removal of the N-terminal segment of IL-18BP promotes the formation of this hetero-tetrameric complex (Fig. 6*C*). We note that Cys51 is part of the N-terminal truncation and likely pairs up with Cys131 in the full-length protein, thus preventing hetero-tetrameric complex formation. Endogenously glycosylated IL-18BP$_{\Delta N}$, without Endo H treatment, also formed a tetrameric complex with IL-18 at high concentrations, albeit at a lower rate than IL-18BP$_{\Delta N\text{-}EH}$ (Fig. 6*D*).

The presence of a cysteine disulfide bridge linking IL-18BP$_{\Delta N}$ and IL-18 distal to the binding interface in the hetero-tetrameric assembly observed here may result in better sequestration and inhibition of IL-18 than in the canonical 1:1 complex. Furthermore, the site where disulfide-linked IL-18BP engages IL-18 would also sterically clash with the eventual binding site of IL-18 to domain 1 of IL-18Rα. To test this, both the heterodimeric or heterotetrameric complex of IL-18BP$_{\Delta N\text{-}EH}$ and IL-18 was purified and used to stimulate KG-1 cells. While both the dimeric and tetrameric complex inhibited IL-18 activity compared to IL-18 alone, the tetrameric assembly restrained IL-18 activity more effectively than the dimeric complex, resulting in less inflammatory cytokine production from KG-1 cells (Fig. 6*E*).

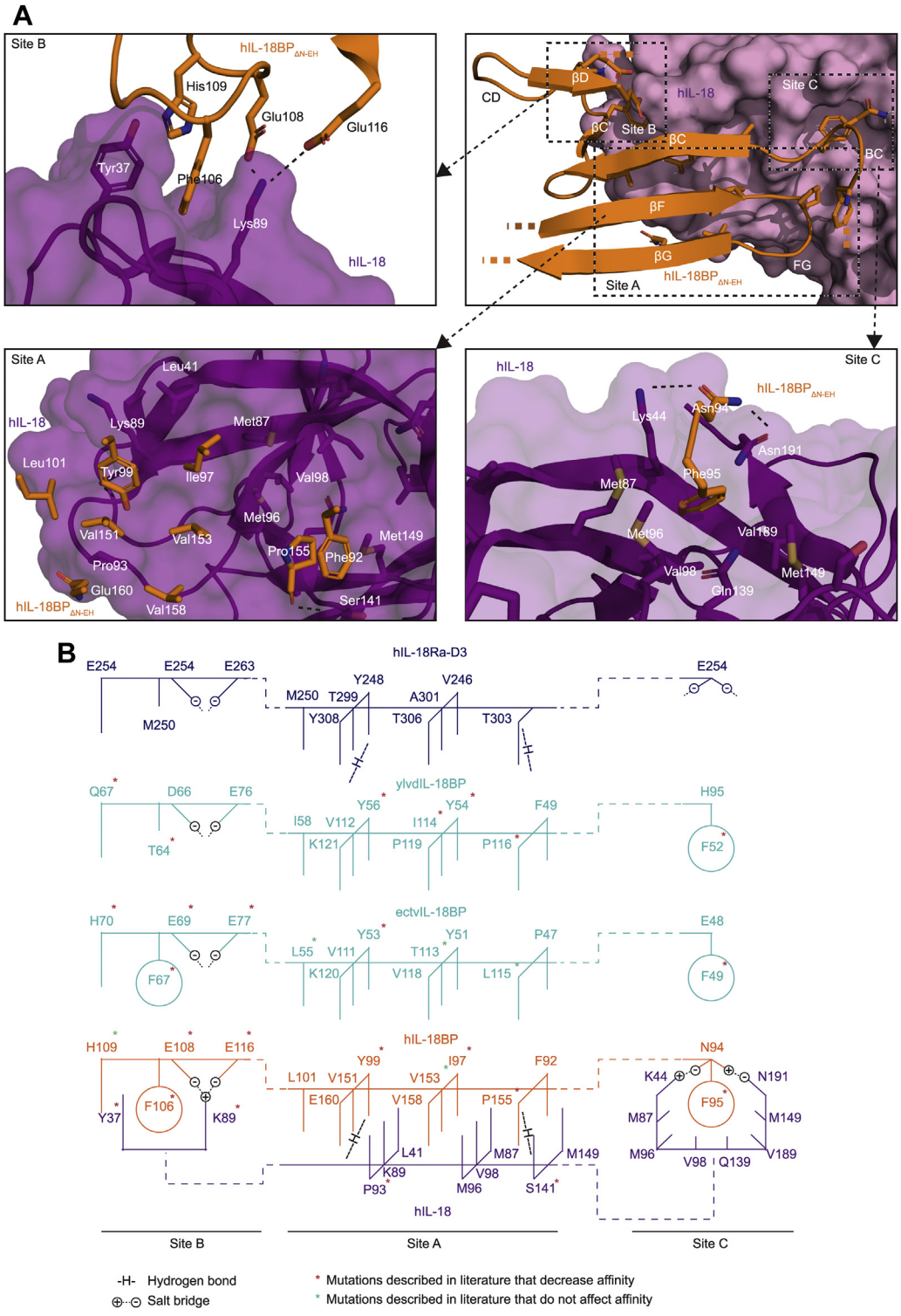

Figure 4. Interaction interface between human IL-18 and human IL-18BP and comparisons with human IL-18 receptor and viral receptor decoys. *A*, *top right panel* shows an overview of interacting structures of hIL-18BPΔN-EH (*cartoon*, *orange*) with hIL-18 (surface, *purple*). Structures of hIL-18BPΔN-EH shown consist out of the *bottom half* of the beta-sandwich, with the *top half* and noninteracting loops hidden. *Top left*, *bottom left*, and *bottom right* panels show zoomed-in views of the three main interaction sites B, *A*, and *C*, respectively, with hIL-18BPΔN-EH and hIL-18 shown in *cartoon* representation with a transparent surface overlay for hIL-18. Key residues are shown in *stick* representation colored by element (*blue*: nitrogen, *red*: oxygen, *yellow*: sulfur, *white*: polar hydrogens, *orange*/*purple*: carbon). Nonpolar hydrogens are hidden. *B*, diagrams show simplified interactions at site A, B, and C of hIL-18 (*purple*) with hIL-18BP (*orange*), viral ectvIL-18BP and ylvdIL-18BP (*cyan*), and domain 3 of hIL-18Rα (*dark blue*). The interaction between hIL-18 and hIL-18BP consists of three sites: A, B, and C. Site A consists of interlocking rows of hydrophobic residues. Site B consist of a phenylalanine flanked by hydrophobic side chains supplemented with two salt bridges. Site C consists of a phenylalanine residing in a large pocket lined by hydrophobic residues supplemented by two salt bridges. Notable differences with ectvIL-18BP and yldvIL-18BP are missing salt bridges at site C, even though a capable side chain is present for ectvIL-18BP. ylvdIL-18BP also has a threonine replacing the phenylalanine at site B. hIL-18Rα -D3 does have the salt bridges at site C but is lacking the phenylalanine with no substitution, while at site B, the phenylalanine is replaced by a methionine. Residues marked with a *red asterisk* have been reported to have reduced affinity after certain mutations. Residues marked with a *green asterisk* have been reported to not be affected by certain mutations. Mutagenesis data were

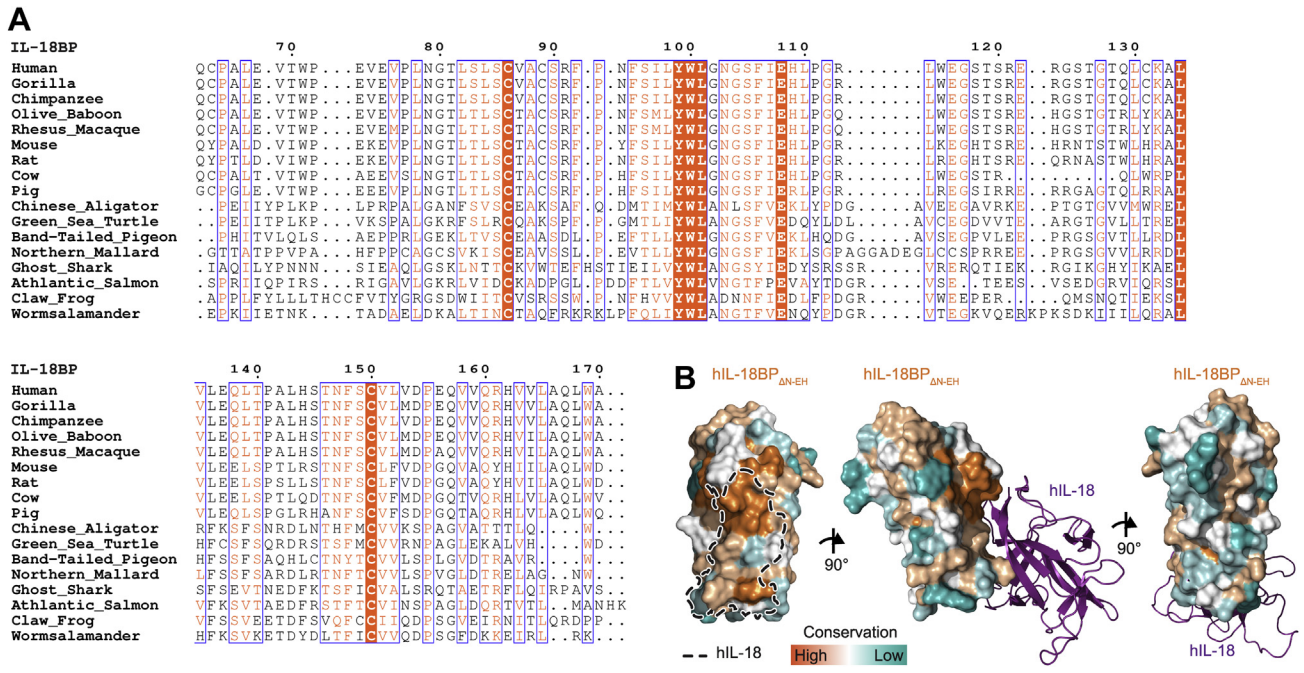

Figure 5. Sequence comparisons and conservation among IL-18BP orthologs. *A*, sequence alignment of core region of orthologous IL-18BPs between species across the animal kingdom. Residues with strict identity have an *orange* background and residues with similarity are colored *orange*. Groups of high similarity residues are surrounded by a *blue box*. Color scale above the sequence of hIL-18BP represents conservation levels determined by ConSurf (85), with high conservation colored in *orange* and low conservation levels in *teal* and *white* in between. The same scale is used in panel B. *B*, surface representation of hIL-18BP$_{\Delta N\text{-}EH}$ colored by residue conservation. hIL-18 binding to hIL-18BP$_{\Delta N\text{-}EH}$ is either displayed in cartoon representation (*purple*, two *right panels*) or shown as a *black dashed line* representing the patch it covers on hIL-18BP$_{\Delta N\text{-}EH}$. IL-18, interleukin-18.

Discussion

Over the past two decades and in the absence of an experimentally determined structure for the human IL-18:IL-18BP complex, numerous studies have used orthogonal methods to predict how human IL-18BP interacts with human IL-18 to efficiently sequester and prevent signaling. To date, structural features and binding interfaces between human IL-18 and human IL-18BP have been inferred from computational models (44), human and viral mutagenesis studies (45–49), and homologous structures of viral IL-18BPs in complex with human IL-18 (22, 23). Additionally, the ternary assembly of human IL-18 in complex with its cognate receptors, IL-18Rα and IL-18Rβ (26), has shed some light on the potential for competitive binding of human IL-18BP. The high-resolution structural analysis of human IL-18BP bound to IL-18 presented here is imperative to further understand and exploit the ultra-high affinity binding mode that characterizes this unique decoy receptor-like protein (22, 23). Human IL-18BP binds the same epitope of hIL-18 used by viral IL-18BPs to compete with the third ectodomain of hIL-18Rα. The interface (site A) predominantly consists of two large, complementary hydrophobic patches, mimicking the landscape of hydrophobic peaks and troughs on each side of the interface, supplemented with two side-chain-to-main-chain hydrogen bonds. Comparing the structure of hIL-18BP with its viral orthologs confirms that this large hydrophobic patch on site A is highly conserved. yldvIL-18BP contains some additional hydrophobic residues (Ile78 and Leu80) on the DE loop interacting with hIL-18 (Leu5 and Glu6) at the perimeter of the interface. In all other structures, except yldvIL-18BP, this loop is constrained as an additional βD′ strand. On each side of the hydrophobic patch, a phenylalanine on hIL-18BP is tightly inserted inside hydrophobic cavities on hIL-18 and additionally locked down by salt bridges (site B and C, Fig. 4*B*). Mutating either phenylalanine residues to alanine reduces the ultra-high picomolar affinity of hIL-18BP down to low-nanomolar affinity (22, 23, 57). Mutations of the corresponding residues in viral IL-18BPs have a similar effect, highlighting the importance of these specific residues for binding. Interestingly, in hIL-18Rα, the corresponding residue is either substituted by methionine (site B) or completely lacking (site C), although site B is flanked by additional hydrophobic residues residing on hIL18 Rα′s longer CD′ loop. The absence of these seemingly critical phenylalanine residues may, in part, explain the higher affinity of hIL-18BP to IL-18 than its receptor. Similarly, mutating Glu108 and Glu106 on hIL-18BP involved in the salt bridges at site B accordingly resulted in a lower affinity, as well as mutating Lys53 on hIL-18 which is located on the other end of the salt bridges (58, 59). Mutations in site C particularly have not been reported, because in both viral structures the corresponding residues (Glu48 in ectvIL-18BP and His51 in yldvIL-18BP) are not involved in salt

adopted from previously reported studies (22, 23, 26, 57, 83, 84). IL-18, interleukin-18; ectvIL-18BP, ectromelia poxvirus IL-18-binding protein; yldvIL-18BP, yaba-like disease virus disease IL-18-binding protein.

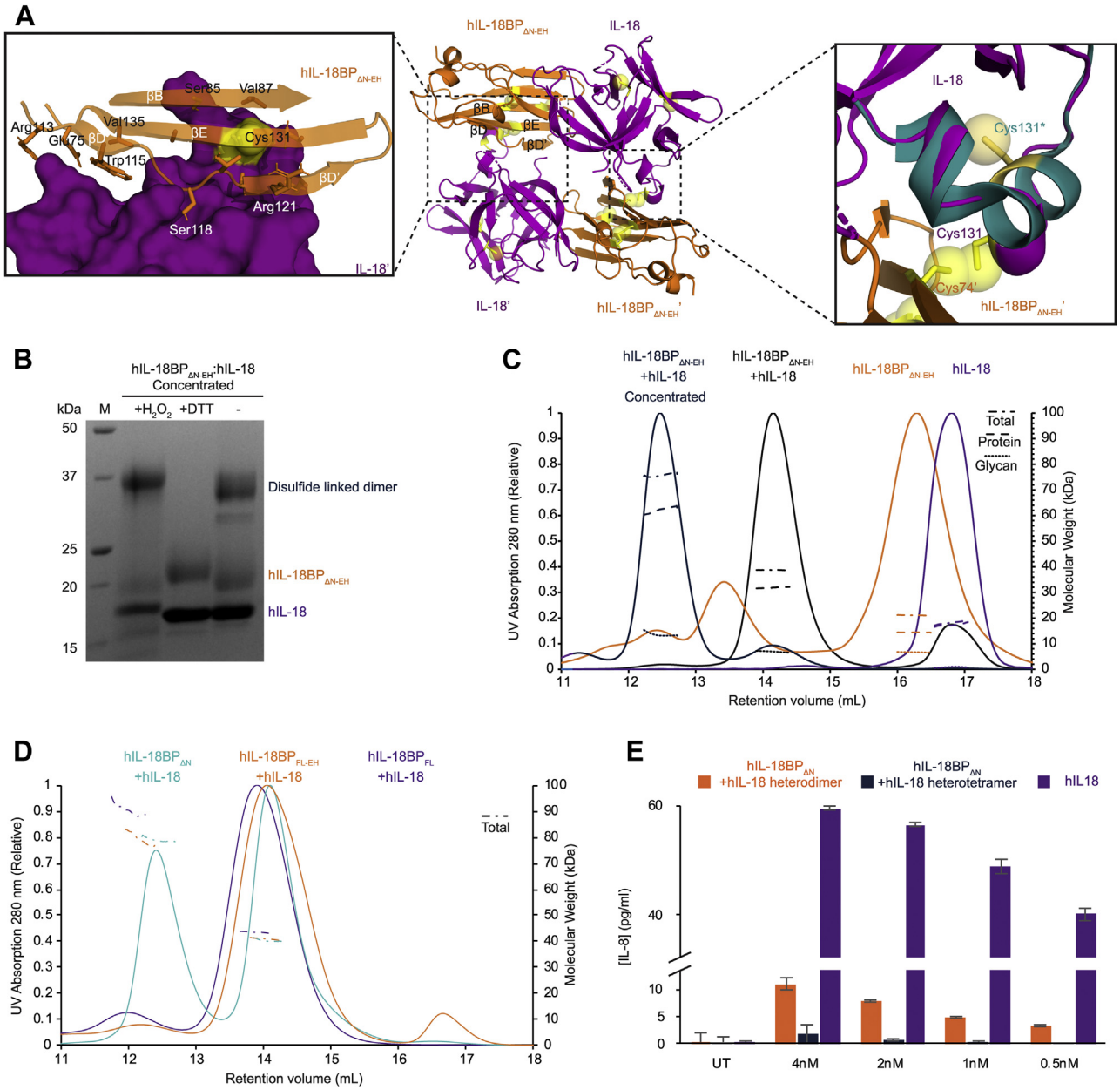

Figure 6. Tetrapartite assembly of human IL-18 and human IL-18BP. *A*, two complexes of hIL-18:hIL-18BP$_{\Delta N\text{-}EH}$ are linked through an intermolecular disulfide bridge between hIL-18 and hIL-18BP$_{\Delta N\text{-}EH}$ from neighboring symmetric related unit forming a hetero-tetrameric assembly with a novel interface. *Middle panel* shows an overview of the assembly using cartoon representation of hIL-18 (*purple* or *teal*) and hIL-18BP$_{\Delta N\text{-}EH}$ (*orange*) with the disulfide links involved shown in *yellow stick* representation. *Left panel* shows a zoomed-in view with an aligned overlay of the 3_{10} α-helix from a crystal structure of unbound hIL-18 (*teal*, pdb 3wo2 (26)), showing disruption of the helix upon formation of the disulfide link. The *right panel* displays the novel interface surrounding the disulfide link with hIL-18 shown in surface representation (*purple*, pdb 7al7) and hIL-18BP$_{\Delta N\text{-}EH}$ in *cartoon* representation (*orange*, pdb 7al7) with key residues displayed in *stick* representation. Secondary structure elements and key residues are labeled accordingly. *B*, SDS-PAGE analysis of hIL-18:hIL-18BP$_{\Delta N\text{-}EH}$ complex sample after concentration to 30 mg/ml prior to crystallization and diluting back to 0.5 mg/ml with oxidizing (H_2O_2), reducing (DTT), or no agents added. Reduction results in dissociation of the otherwise disulfide-linked tetramer. *C*, SEC-MALLS analysis of hIL-18, hIL-18BP$_{\Delta N\text{-}EH}$, and hIL-18:hIL-18BP$_{\Delta N\text{-}EH}$ complex before and after concentration to 30 mg/ml prior to and diluting back to 0.5 mg/ml. Line plots show the SEC retention profile of samples detected by UV (*left axis*). Interrupted lines plot the molecular weights of the sample over the course of the SEC peak, dissected by protein conjugate analysis in total (*dashed* and *dotted*), protein (*dashed*), and glycan (*dotted*) mass (*right axis*). *D*, SEC-MALLS analysis of hIL-18:hIL-18BP$_{\Delta N}$ and hIL-18:hIL-18BP$_{FL}$ complex sample after concentration to 30 mg/ml and diluting back to 0.5 mg/ml. Line plots show the SEC retention profile of samples detected by UV (*left axis*). Interrupted lines plot the molecular weights of the sample over the course of the SEC peak, dissected by protein conjugate analysis in total (*dashed* and *dotted*), protein (*dashed*) and glycan (*dotted*) mass (*right axis*). *E*, bar plot of IL-8 levels (y-axis, pg/ml) in conditioned media after human IL-18 stimulation in presence or absence of dimeric or tetrameric IL-18BP$_{\Delta N\text{-}EH}$:IL-18 complex. Recombinant IL-18 was preincubated for 1 h at 37 °C with the indicated concentrations of full-length IL-18BP or IL-18BP$_{\Delta N\text{-}EH}$. KG-1 cells were left untreated (UT) or stimulated with IL-18 (*purple*) (0.5 nM final concentration) ± IL-18BP (*teal* and *orange*), as indicated. After 18 h, IL-8 concentration in cell culture supernatants was measured by ELISA. Error bars display standard deviation (SEM). IL-18, interleukin-18; SEC, size-exclusion chromatography; MALLS, multi-angle laser light scattering.

bridge formation. Overall, hIL-18BP utilizes a unique constellation of key residues contributing to ultra-high affinity binding to IL-18, however further investigation is required to determine binding hotspots important for this interaction. Whether the lower affinity of viral IL-18BPs is advantageous or disadvantageous for their function remains unclear.

Unexpectedly, we observed a higher order assembly of IL-18 and IL-18BP in our crystallographic model, coordinated by an otherwise buried cysteine in IL-18, disrupting an alpha helix in the process. Using SEC-MALLS and mass spectrometry, we confirmed the formation of a heterotetramer, consisting of two complexes of IL-18:IL-18BP, with an additional interaction interface distal to the canonical-binding site of IL-18BP. Interestingly, this heterotetrameric complex restrained IL-18 activity more effectively than the canonical dimeric 1:1 complex. Given that high concentration and the removal of the N-terminal region appear to be required, it is likely that the observed oligomeric state is not biologically relevant. However, this fortuitous observation suggests that this interface may be amenable to further engineering to increase the sequestration potency of IL-18BP, possibly in combination with domains 1 and 2 of IL-18Rα. It brings to light plasticity in IL-18, the possible reactivity of Cys131 in IL-18BP, and the possible utilization of a hydrophobic patch at opposite ends to the IL-18:IL-18BP interface to create a new interaction interface. An analogous yet distinct bivalence has been observed in viral yldvIL-18BP. This ortholog lacks a highly conserved phenylalanine residue in site B, however it compensates for this by forming a 2:2 complex with IL-18, driven by disulfide-linked IL-18BP homodimerization (23). However, we note that the 2:2 heterotetrameric complex seen here for human IL-18BP engages a separate interface and is driven by an additional interaction with IL-18.

The structural model presented here will further facilitate the structure-driven development of novel therapeutics to either disrupt or mimic hIL-18BP binding. Aberrant IL-18 signaling has been implicated in numerous inflammatory diseases including RA, AOSD, systemic lupus erythematosus, sickle cell disease, and more recently, the inflammatory phase of coronavirus infection (28, 29, 36, 37, 60). Coronavirus disease (COVID-19), caused by the SARS-CoV2 virus, displays a broad range of clinical symptoms, resulting in disease severity extending from mild to fatal outcomes. Accumulating evidence has shown that tissue damage in the later stages of severe COVID-19 infection is driven by cytokine release syndrome, also known as cytokine storm (38, 39, 61). Recent studies have detected elevated levels of IL-18 in patients with moderate and severe COVID-19 infection, which strongly correlated with disease severity (38, 39, 62). Longitudinal analysis of patients infected with SARS-CoV-2 showed IL-18 levels remained elevated in severe COVID-19 patients admitted to ICU, while cytokine levels declined over time in moderately affected patients. Moreover, both IL-18 and IL-18BP have been identified as promising biomarkers to predict disease severity and likelihood of death after SARS-CoV-2 infection (38, 63). Elevated levels of IL-18 were also detected in multisystem inflammatory syndrome and Kawasaki syndrome in children following SARS-CoV-2 infection and may be used as a biomarker to distinguish these diseases from similar hyperinflammatory syndromes (37). Increased IL-18 production has also been associated with activation of cytotoxic mucosal-associated invariant T cells during coronavirus infection, leading to lung tissue damage and increased disease severity (40). These studies suggest that modulation of IL-18 activity may represent a novel therapeutic opportunity for COVID-19, however, no clinical trials with recombinant IL-18BP or IL-18-specific antagonistic have yet been initiated (64, 65). However, because of the pleiotropic activity of IL-18, there will likely be a narrow therapeutic window to exploit the beneficial activity of IL-18 for effective viral clearance, while avoiding aberrant inflammation and tissue damage associated with high IL-18 activity during late-stage infection. In addition, IL-18 has been shown to display potent antitumor activity, however clinical trials using recombinant IL-18 have shown limited efficacy (42). IL-18BP, produced in the tumor microenvironment, has been identified as an 'immune checkpoint', hampering the therapeutic application of recombinant IL-18 in cancer (66). Directed evolution of yeast-displayed mouse IL-18 variants identified a decoy-resistant IL-18 that retains signaling activity but escapes inhibition by IL-18BP. This IL-18 variant displayed potent cytotoxic T cell activation, NK cell maturation, and tumor growth inhibition compared to its WT counterpart (66). The high-resolution structural models presented here, in particular the experimentally determined interaction interface of IL-18 and human IL-18BP, will be of crucial importance for additional protein engineering and future drug design for the development of novel therapeutics for use in viral infections, autoimmune and inflammatory diseases, and cancer.

Experimental procedures

Plasmids, protein expression constructs, and cell lines

All constructs were created by a traditional restriction ligation approach. Restriction enzymes, T4 ligase, and Q5 polymerase were purchased from NEB (New England Biolabs). All primers were purchased from IDT (Integrated DNA Technologies). Recombinant DNA was purchased from GenScript. The mature sequence of human IL-18 (residues 37–193, UniProt ID: Q14116) was codon optimized for expression in *E. coli* and purchased in the pUC57 vector from GenScript. The sequence was cloned into the pET42a plasmid (Cat No 70561, Novagen, Merck) in frame with an N-terminal caspase 3-cleavable glutathione S-transferase (GST)-tag (26). The introduction of an extra N-terminal hexahistidine (His_6)-tag was performed by PCR. The sequence of human IL-18BP (residues 1–194, UniProt ID: O95998) was purchased in the pUC57 vector at GenScript. The sequence was cloned in frame with a C-terminal caspase 3 site followed by an AviTag and a His_6 tag. The construct was further cloned in frame with an N-terminal chicken RTPμ-like signal peptide sequence (67) that replaced the native signal peptide sequence (residues 1–30). For crystallization purposes, the N-terminus (residues 31–60) was removed by PCR (IL-18$BP_{\Delta N}$) and the construct

was cloned in the same pHLSec plasmid containing an N-terminal chicken RTPμ-like signal peptide sequence and a caspase 3 cleavable Avi-His_6-tag. All constructs were validated by Sanger sequencing by GATC BioTech before further experiments were performed.

Expression and purification of recombinant proteins

BL21(DE3) *E. coli* transformed with plasmid pET42 expressing N-terminally GST- and HIS-tagged human IL-18 were grown at 37 °C in LB medium containing kanamycin (25 μg/ml) as selection marker for the pET42a plasmid (Cat No 70561, Novagen, Merck). When the optical density at 600 nm (A600) reached 0.6, the expression of human IL-18 was induced by addition of ITPG at a final concentration of 1 mM, after which the culture was incubated at 28 °C for 5 h. The bacteria were harvested by centrifugation (7000*g* for 10 min at 4 °C) and the cellular pellet was stored at −80 °C. The bacterial pellet was thawed and resuspended in Hepes-buffered saline (HBS, 20 mM Hepes, 150 mM NaCl, pH 7.4) with DNaseI (REF 10104159001, Roche Diagnostics). The cells were lysed by sonication with a Qsonica macrotip sonicator) (on-time 4 min; pulse on 30 s; pulse off 30 s; amplitude 70%) while cooled on ice. The lysate was clarified by centrifugation (20,000*g* for 45 min at 4 °C) and filtration using a 0.22-μm Millipore Steritop Sterile Vacuum Bottle-Top Filter (Thermo Fisher Scientific) and loaded onto a HisTrap HP 5 ml column (GE Healthcare) equilibrated with HBS. The column was washed (HBS, 50 mM imidazole) before eluting the protein (HBS, 250 mM imidazole) following desalting using a HiPrep 26/10 Desalting column (GE Healthcare) to remove imidazole. The His_6-GST-tag was removed by caspase 3 (produced in-house) cleavage at 37 °C for 1 h. To remove the uncleaved protein and the His_6-GST-tag, the sample was again loaded onto a HisTrap HP 5 ml column (GE Healthcare). The flow-through was collected and concentrated before injection onto a HiLoad 16/600 Superdex 75 pg column (GE Healthcare) using HBS as running buffer. Fractions containing human IL-18 were pooled, flash frozen, and stored at −80 °C. The purity of the protein was evaluated on SDS-PAGE stained with Coomassie blue.

Expression and purification of recombinant human IL-18BP

Adherent HEK293S MGAT1$^{-/-}$ cells (68) were grown in 5-layer cell culture flasks (Falcon Multi-Flask, Corning) in Dulbecco's Modified Eagle Medium (DMEM) (Gibco, Life Technologies, Thermo Fisher Scientific), supplemented with 10% fetal calf serum (Bodinco). Upon transfection, the growth medium was exchanged for DMEM supplemented with 3.6 mM valproic acid (item 13033, Cayman Chemical Company). Transient expression of human IL-18BP or IL-$18BP_{\Delta N}$ was achieved using branched PEI (Mn ∼ 10000, Cat.:40872-7, Sigma-Aldrich) as transfection reagent (67). After 4 days of expression, filtered conditioned medium was loaded onto a 5 ml cOmplete His-tag Purification Column (Roche Diagnostics). The protein was eluted with 250 mM imidazole in HBS after which the imidazole was removed using a HiPrep 26/10 Desalting column (GE Healthcare). The Avi-His_6-tag was cleaved by caspase-3 (produced in-house) and the glycans were trimmed by Endo H (produced in-house) at 37 °C for 1 h. The flow-through of the HisTrap HP 5 ml column (GE Healthcare) containing the cleaved protein was concentrated and injected onto a HiLoad 16/600 Superdex 200 pg column (GE Healthcare Life Sciences) using HBS as running buffer. Fractions containing human IL-18BP or IL-$18BP_{\Delta N}$ were pooled, flash frozen, and stored at −80 °C. The purity of the protein was evaluated on SDS-PAGE stained with Coomassie.

Multi-angle laser light scattering

Purified protein samples at a concentration of 0.5 mg ml^{-1} were injected onto a Superdex Increase 10/300 Gl column (GE Healthcare) that was pre-equilibrated with HBS. The column was coupled in line with a UV-detector (Shimadzu), a miniDAWN TREOS MALLS detector (Wyatt) and an Optilab T-rEX refractometer (Wyatt). Refractive index increment values (dn/dc) of 0.185 ml g^{-1} and 0.155 ml g^{-1} were used for protein and glycan analysis, respectively. Bovine serum albumin (Pierce) was used as standard to correct for band broadening. The resulting data was analyzed using the ASTRA6.1 software (Wyatt, v6.1) and errors were calculated in Microsoft Excel.

Isothermal titration calorimetry

All proteins were buffer matched in HBS from the same batch using SEC and all the solutions were degassed. Protein concentrations were determined with the NanoDrop 2000 (Thermo Fisher Scientific) using their corresponding extinction coefficients (absorbance of 1%). Experiments were carried out on the MicroCal VP-ITC calorimeter (Malvern Panalytical) at 37 °C. Titrations were always preceded by an initial injection of 3 μl and were carried out using 10 μl injections applied 300 s apart. The sample was stirred at a speed of 300 r.p.m. throughout. The data was recorded using the Origin scientific plotting software (Version 7.0, MicroCal, Malvern Panalytical) and further analyzed using NITPIC (69) and SEDPHAT (70) fitting the data with a "one to one" binding model.

Bioactivity assays

KG-1 cells were cultured in RPMI media (Gibco) supplemented with 10 % fetal calf serum (Bodinco). Cells were cultured at 37 °C in a humidified atmosphere with 5% CO_2. KG-1 cells were plated at 2 × 10^5 cells per well in 24-well plates. Recombinant IL-18 was preincubated with IL-$18BP_{FL}$, IL-$18BP_{\Delta N\text{-}EH}$, or complexes thereof as indicated, for 1 h at 37 °C. KG-1 cells were left untreated or stimulated with IL-18 (0.5 nM final concentration) ± IL-18BP, as indicated. Cells were incubated with stimuli for 18 h, and cell culture supernatants were subsequently collected. Culture supernatants were centrifuged for 5 min at 1000*g* to remove cells and frozen at −80 °C.

Detection of cytokines by ELISA

Human IL-8 was measured from cell culture supernatants using commercially available specific paired ELISA kits (R&D Systems). Briefly, a 96-well plate was coated with 50 ml of capture antibody per well according to manufacturer's instructions and incubated overnight at room temperature. Wells were washed three times with 150 ml wash buffer (0.05% Tween-20 in PBS, pH 7.2), then blocked for 1 h in reagent diluent (1% bovine serum albumin in PBS, pH 7.2). Samples were diluted as required in reagent diluent, and 50 ml of each sample was added to wells and incubated for 2 h at room temperature. Appropriate standards were prepared for each ELISA assay according to manufacturer's instructions. Wells were washed again three times, followed by 50 ml of biotin-conjugated detection antibody incubated for 2 h. Wells were washed three times, and 50 ml streptavidin-HRP was added to wells and incubated for 30 min in the dark. Finally, wells were washed three times, followed by addition of 50 ml TMB substrate solution. The reaction was stopped with 30 ml of 2M sulfuric acid and absorbance was read at 450 nm on an ELISA plate reader (Fluostar). All cytokine assays were carried out using triplicate samples from each culture.

Bioinformatic analyses

All sequence alignments were performed by Clustal Omega (71). Structural alignments were performed in Swiss-PdbViewer (72). Glycan prediction was performed using NetNGlyc (73) and NetOGlyc servers (74). Protein disorder was predicted using IUPred (75). Sequence alignments were visualized by ESPript (76). Protein structures were visualized in PyMOL (77). Interaction interfaces were inferred using the PISA server (78).

Crystal structure determination and refinement

During the purification of IL-18BP$_{\Delta N}$, purified IL-18 was added in a 1:2 ratio prior to caspase 3 and Endo H digests. The complex was purified *via* SEC and concentrated to 35 mgml^{-1}. Sitting-drop vapor diffusion experiments were set up in Swissci 96-well triple drop plates (Molecular dimensions) with commercial sparse matrix crystallization screens. Using a Mosquito liquid handling robot (TTP Labtech), the protein was mixed with mother liquor in a 1:1 ratio in a final volume of 200 nl. The plates were incubated at 20 °C. An initial hit in the Crystal Screen (Cat No HR2-110, Hampton Research) in condition D10 (0.2 M calcium acetate hydrate, 0.1 M sodium cacodylate trihydrate pH 6.5, 18% w/v polyethylene glycol 8000) was optimized by varying pH (6.2–7.1) and PEG concentration (12%–27%). Crystals obtained from the optimization screen were used for seeding new plates, finally yielding single crystals. These crystals were cryoprotected in mother liquor supplemented with 20% glucose prior to cryocooling in liquid nitrogen. Diffraction data was initially collected under cryogenic conditions at a beamline P14 of synchrotron PETRA III (Hamburg, Germany).

The diffraction data were integrated using XDS (79) and were treated for anisotropy using the STARANISO server (55). Initial phases were determined by maximum-likelihood molecular replacement in PHASER (80) using a search model derived from the structure of hIL-18 in complex with ectvhIL-18BP (pdb 3f62). Iterative cycles of structure building and refinement were performed in COOT (81) and PHENIX.refine (82), respectively.

Structure coordinates and structure factors for the human IL-18:IL18BP complex have been deposited in the Protein Data Bank (PDB) under accession code 7al7.

Data availability

Structure coordinates and structure factors for the human IL-18:IL18BP complex have been deposited in the Protein Data Bank (PDB) under accession code 7al7.

Acknowledgments—We thank AB2 Bio Ltd (Lausanne, Switzerland) for clinical grade recombinant IL-18BP and Prof. Seamus Martin, Trinity College (Dublin, Ireland) for providing KG-1 cells. This project has received funding from the European Union's Horizon 2020 research and innovation program under grant agreement No 779295. We gratefully acknowledge the staff of beamlines P13/14 at synchrotron PETRA III (Hamburg, Germany) and Proxima 1/2A at synchrotron SOLEIL (France) for the allocation of beamtime and expert technical support.

Author contributions—S. D., J. A., and D. M. C. investigation; S. D., J. A., Y. B., and D. M. C. methodology; S. D., J. A., and D. M. C. validation; S. D., J. A., and D. M. C. formal analysis; S. D., J. A., D. M. C., and S. N. S. data curation; S. D., J. A., D. M. C., and S. N. S. writing–original draft; S. D., J. A., Y. B., C. G., D. M. C., and S. N. S. writing–review and editing; C. G. resources; S. N. S. conceptualization; S. N. S. supervision; S. N. S. funding acquisition; S. N. S. project administration.

Funding and additional information—J. A., Y. B., and D. M. C. are research fellows of Research Foundation Flanders (FWO), Belgium.

Conflict of interest—The authors declare that they have no conflicts of interest with the contents of this article.

Abbreviations—The abbreviations used are: AOSD, Adult-onset Still's disease; CD, Crohn's disease; COVID-19, Coronavirus disease; ectvIL-18BP, ectromelia poxvirus IL-18-binding protein; Endo H, Endoglycosidase H; HBS, Hepes-buffered saline; IFN-γ, interferon-γ; IL-18, interleukin-18; MALLS, multi-angle laser light scattering; RA, rheumatoid arthritis; SEC, size-exclusion chromatography; yldvIL-18BP, yaba-like disease virus disease IL-18-binding protein.

References

1. Okamura, H., Kawaguchi, K., Shoji, K., and Kawade, Y. (1982) High-level induction of gamma interferon with various mitogens in mice pretreated with Propionibacterium acnes. *Infect. Immun.* **38**, 440–443
2. Wada, M., Okamura, H., Nagata, K., Shimoyama, T., and Kawade, Y. (1985) Cellular mechanisms in *in vivo* production of gamma interferon induced by lipopolysaccharide in mice infected with Mycobacterium bovis BCG. *J. Interferon Res.* **5**, 431–443
3. Nakamura, K., Okamura, H., Wada, M., Nagata, K., and Tamura, T. (1989) Endotoxin-induced serum factor that stimulates gamma interferon production. *Infect. Immun.* **57**, 590–595

4. Ushio, S., Namba, M., Okura, T., Hattori, K., Nukada, Y., Akita, K., Tanabe, F., Konishi, K., Micallef, M., Fujii, M., Torigoe, K., Tanimoto, T., Fukuda, S., Ikeda, M., Okamura, H., *et al.* (1996) Cloning of the cDNA for human IFN-gamma-inducing factor, expression in Escherichia coli, and studies on the biologic activities of the protein. *J. Immunol.* **156**, 4274–4279
5. Ghayur, T., Banerjee, S., Hugunin, M., Butler, D., Herzog, L., Carter, A., Quintal, L., Sekut, L., Talanian, R., Paskind, M., Wong, W., Kamen, R., Tracey, D., and Allen, H. (1997) Caspase-1 processes IFN-gamma-inducing factor and regulates LPS-induced IFN-gamma production. *Nature* **386**, 619–623
6. Gu, Y., Kuida, K., Tsutsui, H., Ku, G., Hsiao, K., Fleming, M. A., Hayashi, N., Higashino, K., Okamura, H., Nakanishi, K., Kurimoto, M., Tanimoto, T., Flavell, R. A., Sato, V., Harding, M. W., *et al.* (1997) Activation of interferon-gamma inducing factor mediated by interleukin-1beta converting enzyme. *Science* **275**, 206–209
7. Dinarello, C. A. (2018) Overview of the IL-1 family in innate inflammation and acquired immunity. *Immunol. Rev.* **281**, 8–27
8. Afonina, I. S., Müller, C., Martin, S. J., and Beyaert, R. (2015) Proteolytic processing of interleukin-1 family cytokines: Variations on a common theme. *Immunity* **42**, 991–1004
9. Medzhitov, R., Preston-Hurlburt, P., Kopp, E., Stadlen, A., Chen, C., Ghosh, S., and Janeway, C. A. (1998) MyD88 is an adaptor protein in the hToll/IL-1 receptor family signaling pathways. *Mol. Cell* **2**, 253–258
10. Wesche, H., Henzel, W. J., Shillinglaw, W., Li, S., and Cao, Z. (1997) MyD88: An adapter that recruits IRAK to the IL-1 receptor complex. *Immunity* **7**, 837–847
11. Cao, Z., Xiong, J., Takeuchi, M., Kurama, T., and Goeddel, D. V. (1996) TRAF6 is a signal transducer for interleukin-1. *Nature* **383**, 443–446
12. Weber, A., Wasiliew, P., and Kracht, M. (2010) Interleukin-1β (IL-1β) processing pathway. *Sci. Signal.* **3**, cm2
13. Dinarello, C. A. (1999) Interleukin-18. *Methods* **19**, 121–132
14. Dinarello, C. A., Novick, D., Kim, S., and Kaplanski, G. (2013) Interleukin-18 and IL-18 binding protein. *Front. Immunol.* **4**, 289
15. Tone, M., Thompson, S. A., Tone, Y., Fairchild, P. J., and Waldmann, H. (1997) Regulation of IL-18 (IFN-gamma-inducing factor) gene expression. *J. Immunol.* **159**, 6156–6163
16. Mantovani, A., Dinarello, C. A., Molgora, M., and Garlanda, C. (2019) Interleukin-1 and related cytokines in the regulation of inflammation and immunity. *Immunity* **50**, 778–795
17. Novick, D., Kim, S.-H., Fantuzzi, G., Reznikov, L. L., Dinarello, C. A., and Rubinstein, M. (1999) Interleukin-18 binding protein: A novel modulator of the Th1 cytokine response. *Immunity* **10**, 127–136
18. Novick, D., Kim, S., Kaplanski, G., and Dinarello, C. A. (2013) Interleukin-18, more than a Th1 cytokine. *Semin. Immunol.* **25**, 439–448
19. Felix, J., and Savvides, S. N. (2017) Mechanisms of immunomodulation by mammalian and viral decoy receptors: Insights from structures. *Nat. Rev. Immunol.* **17**, 112–129
20. Xiang, Y., and Moss, B. (1999) IL-18 binding and inhibition of interferon gamma induction by human poxvirus-encoded proteins. *Proc. Natl. Acad. Sci. U. S. A.* **96**, 11537–11542
21. Born, T. L., Morrison, L. A., Esteban, D. J., VandenBos, T., Thebeau, L. G., Chen, N., Spriggs, M. K., Sims, J. E., and Buller, R. M. L. (2000) A poxvirus protein that binds to and inactivates IL-18, and inhibits NK cell response. *J. Immunol.* **164**, 3246–3254
22. Krumm, B., Meng, X., Li, Y., Xiang, Y., and Deng, J. (2008) Structural basis for antagonism of human interleukin 18 by poxvirus interleukin 18-binding protein. *Proc. Natl. Acad. Sci. U. S. A.* **105**, 20711–20715
23. Krumm, B., Meng, X., Wang, Z., Xiang, Y., and Deng, J. (2012) A unique bivalent binding and inhibition mechanism by the yatapoxvirus interleukin 18 binding protein. *PLoS Pathog.* **8**, e1002876
24. Novick, D., Schwartsburd, B., Pinkus, R., Suissa, D., Belzer, I., Sthoeger, Z., Keane, W. F., Chvatchko, Y., Kim, S.-H., Fantuzzi, G., Dinarello, C. A., and Rubinstein, M. (2001) A novel IL-18BP ELISA shows elevated serum IL-18BP in sepsis and extensive decrease of free IL-18. *Cytokine* **14**, 334–342
25. Calderara, S., Xiang, Y., and Moss, B. (2001) Orthopoxvirus Il-18 binding proteins: Affinities and antagonist activities. *Virology* **279**, 22–26
26. Tsutsumi, N., Kimura, T., Arita, K., Ariyoshi, M., Ohnishi, H., Yamamoto, T., Zuo, X., Maenaka, K., Park, E. Y., Kondo, N., Shirakawa, M., Tochio, H., and Kato, Z. (2014) The structural basis for receptor recognition of human interleukin-18. *Nat. Commun.* **5**, 5340
27. Mühl, H., Kämpfer, H., Bosmann, M., Frank, S., Radeke, H., and Pfeilschifter, J. (2000) Interferon-γ mediates gene expression of IL-18 binding protein in nonleukocytic cells. *Biochem. Biophys. Res. Commun.* **267**, 960–963
28. Harel, M., Girard-Guyonvarc'h, C., Rodriguez, E., Palmer, G., and Gabay, C. (2020) Production of IL-18 binding protein by radiosensitive and radioresistant cells in CpG-induced macrophage activation syndrome. *J. Immunol.* **205**, 1167–1175
29. Yamamura, M., Kawashima, M., Taniai, M., Yamauchi, H., Tanimoto, T., Kurimoto, M., Morita, Y., Ohmoto, Y., and Makino, H. (2001) Interferon-?-inducing activity of interleukin-18 in the joint with rheumatoid arthritis. *Arthritis Rheum.* **44**, 275–285
30. Tanaka, M., Harigai, M., Kawaguchi, Y., Ohta, S., Sugiura, T., Takagi, K., Ohsako-Higami, S., Fukasawa, C., Hara, M., and Kamatani, N. (2001) Mature form of interleukin 18 is expressed in rheumatoid arthritis synovial tissue and contributes to interferon-gamma production by synovial T cells. *J. Rheumatol.* **28**, 1779–1787
31. Monteleone, G., Trapasso, F., Parrello, T., Biancone, L., Stella, A., Iuliano, R., Luzza, F., Fusco, A., Pallone, F., and Takada, H. (1999) Bioactive IL-18 expression is up-regulated in Crohn's disease. *J. Immunol.* **163**, 143–147
32. Pizarro, T. T., Michie, M. H., Bentz, M., Woraratanadharm, J., Smith, M. F., Foley, E., Moskaluk, C. A., Bickston, S. J., and Cominelli, F. (1999) IL-18, a novel immunoregulatory cytokine, is up-regulated in Crohn's disease: Expression and localization in intestinal mucosal cells. *J. Immunol.* **162**, 6829–6835
33. Csiszár, A., Nagy, G., Gergely, P., Pozsonyi, T., and Pócsik, E. (2000) Increased interferon-gamma (IFN-gamma), IL-10 and decreased IL-4 mRNA expression in peripheral blood mononuclear cells (PBMC) from patients with systemic lupus erythematosus (SLE). *Clin. Exp. Immunol.* **122**, 464–470
34. Wong, C. K., Li, E. K., Ho, C. Y., and Lam, C. W. (2000) Elevation of plasma interleukin-18 concentration is correlated with disease activity in systemic lupus erythematosus. *Rheumatol* **39**, 1078–1081
35. Novick, D., Elbirt, D., Miller, G., Dinarello, C. A., Rubinstein, M., and Sthoeger, Z. M. (2010) High circulating levels of free interleukin-18 in patients with active SLE in the presence of elevated levels of interleukin-18 binding protein. *J. Autoimmun.* **34**, 121–126
36. Girard, C., Rech, J., Brown, M., Allali, D., Roux-Lombard, P., Spertini, F., Schiffrin, E. J., Schett, G., Manger, B., Bas, S., del Val, G., and Gabay, C. (2016) Elevated serum levels of free interleukin-18 in adult-onset Still's disease. *Rheumatology (Oxford)* **55**, 2237–2247
37. Rodriguez-Smith, J. J., Verweyen, E. L., Clay, G. M., Esteban, Y. M., de Loizaga, S. R., Baker, E. J., Do, T., Dhakal, S., Lang, S. M., Grom, A. A., Grier, D., and Schulert, G. S. (2021) Inflammatory biomarkers in COVID-19-associated multisystem inflammatory syndrome in children, Kawasaki disease, and macrophage activation syndrome: A cohort study. *Lancet Rheumatol.* **3**, e574–e584
38. Lucas, C., Wong, P., Klein, J., Castro, T. B. R., Silva, J., Sundaram, M., Ellingson, M. K., Mao, T., Oh, J. E., Israelow, B., Takahashi, T., Tokuyama, M., Lu, P., Venkataraman, A., Park, A., *et al.* (2020) Longitudinal analyses reveal immunological misfiring in severe COVID-19. *Nature* **584**, 463–469
39. Huang, W., Li, M., Luo, G., Wu, X., Su, B., Zhao, L., Zhang, S., Chen, X., Jia, M., Zhu, J., Su, W., and Zhang, D. (2021) The inflammatory factors associated with disease severity to predict COVID-19 progression. *J. Immunol.* **206**, 1597–1608
40. Flament, H., Rouland, M., Beaudoin, L., Toubal, A., Bertrand, L., Lebourgeois, S., Rousseau, C., Soulard, P., Gouda, Z., Cagninacci, L., Monteiro, A. C., Hurtado-Nedelec, M., Luce, S., Bailly, K., Andrieu, M., *et al.* (2021) Outcome of SARS-CoV-2 infection is linked to MAIT cell activation and cytotoxicity. *Nat. Immunol.* **22**, 322–335
41. Clark, D. N., Markham, J. L., Sloan, C. S., and Poole, B. D. (2013) Cytokine inhibition as a strategy for treating systemic lupus erythematosus. *Clin. Immunol.* **148**, 335–343

42. Ten Hove, T., Corbaz, A., Amitai, H., Aloni, S., Belzer, I., Graber, P., Drillenburg, P., van Deventer, S. J., Chvatchko, Y., and Te Velde, A. A. (2001) Blockade of endogenous IL-18 ameliorates TNBS-induced colitis by decreasing local TNF-alpha production in mice. *Gastroenterology* **121**, 1372–1379
43. Gabay, C., Fautrel, B., Rech, J., Spertini, F., Feist, E., Kötter, I., Hachulla, E., Morel, J., Schaeverbeke, T., Hamidou, M. A., Martin, T., Hellmich, B., Lamprecht, P., Schulze-Koops, H., Courvoisier, D. S., *et al.* (2018) Open-label, multicentre, dose-escalating phase II clinical trial on the safety and efficacy of tadekinig alfa (IL-18BP) in adult-onset Still's disease. *Ann. Rheum. Dis.* **77**, 840–847
44. Tak, P. P., Bacchi, M., and Bertolino, M. (2006) Pharmacokinetics of IL-18 binding protein in healthy volunteers and subjects with rheumatoid arthritis or plaque psoriasis. *Eur. J. Drug Metab. Pharmacokinet.* **31**, 109–116
45. Ma, Z., Li, W., Yoshiya, S., Xu, Y., Hata, M., El-Darawish, Y., Markova, T., Yamanishi, K., Yamanishi, H., Tahara, H., Tanaka, Y., and Okamura, H. (2016) Augmentation of immune checkpoint cancer immunotherapy with IL18. *Clin. Cancer Res.* **22**, 2969–2980
46. Robertson, M. J., Mier, J. W., Logan, T., Atkins, M., Koon, H., Koch, K. M., Kathman, S., Pandite, L. N., Oei, C., Kirby, L. C., Jewell, R. C., Bell, W. N., Thurmond, L. M., Weisenbach, J., Roberts, S., *et al.* (2006) Clinical and biological effects of recombinant human interleukin-18 administered by intravenous infusion to patients with advanced cancer. *Clin. Cancer Res.* **12**, 4265–4273
47. Tarhini, A. A., Millward, M., Mainwaring, P., Kefford, R., Logan, T., Pavlick, A., Kathman, S. J., Laubscher, K. H., Dar, M. M., and Kirkwood, J. M. (2009) A phase 2, randomized study of SB-485232, rhIL-18, in patients with previously untreated metastatic melanoma. *Cancer* **115**, 859–868
48. Robertson, M. J., Kirkwood, J. M., Logan, T. F., Koch, K. M., Kathman, S., Kirby, L. C., Bell, W. N., Weisenbach, J., Thurmond, L. M., and Dar, M. M. (2008) A dose-escalation study of recombinant human Lnterleukin-18 using two different schedules of administration in patients with cancer. *Clin. Cancer Res.* **14**, 3462–3469
49. Reeves, P. J., Thurmond, R. L., and Khorana, H. G. (1996) Structure and function in rhodopsin: High level expression of a synthetic bovine opsin gene and its mutants in stable mammalian cell lines. *Proc. Natl. Acad. Sci. U. S. A.* **93**, 11487–11492
50. Elegheert, J., Bracke, N., Pouliot, P., Gutsche, I., Shkumatov, A. V., Tarbouriech, N., Verstraete, K., Bekaert, A., Burmeister, W. P., Svergun, D. I., Lambrecht, B. N., Vergauwen, B., and Savvides, S. N. (2012) Allosteric competitive inactivation of hematopoietic CSF-1 signaling by the viral decoy receptor BARF1. *Nat. Struct. Mol. Biol.* **19**, 938–947
51. Felix, J., De Munck, S., Verstraete, K., Meuris, L., Callewaert, N., Elegheert, J., and Savvides, S. N. (2015) Structure and assembly mechanism of the signaling complex mediated by human CSF-1. *Structure* **23**, 1621–1631
52. Bloch, Y., Bouchareychas, L., Merceron, R., Składanowska, K., Van den Bossche, L., Detry, S., Govindarajan, S., Elewaut, D., Haerynck, F., Dullaers, M., Adamopoulos, I. E., Savvides, S. N., Skladanowska, K., Van den Bossche, L., Detry, S., *et al.* (2018) Structural activation of pro-inflammatory human cytokine IL-23 by cognate IL-23 receptor enables recruitment of the shared receptor IL-12rβ1. *Immunity* **48**, 45–58.e6
53. Felix, J., Kandiah, E., De Munck, S., Bloch, Y., van Zundert, G. C. P., Pauwels, K., Dansercoer, A., Novanska, K., Read, R. J., Bonvin, A. M. J. J., Vergauwen, B., Verstraete, K., Gutsche, I., and Savvides, S. N. (2016) Structural basis of GM-CSF and IL-2 sequestration by the viral decoy receptor GIF. *Nat. Commun.* **7**, 13228
54. Fukushima, K., Ikehara, Y., and Yamashita, K. (2005) Functional role played by the glycosylphosphatidylinositol anchor glycan of CD48 in interleukin-18-induced interferon-γ production. *J. Biol. Chem.* **280**, 18056–18062
55. Vorhein, C., Tickle, I. J., Flensburg, C., Keller, P., Paciorek, W., Sharff, A., and Bricogne, G. (2018) Advances in automated data analysis and processing within *autoPROC*, combined with improved characterisation, mitigation and visualisation of the anisotropy of diffraction limits using *STARANISO*. *Acta Crystallographica A* **A74**. a360–a360
56. Kato, Z., Jee, J. G., Shikano, H., Mishima, M., Ohki, I., Ohnishi, H., Li, A., Hashimoto, K., Matsukuma, E., Omoya, K., Yamamoto, Y., Yoneda, T., Hara, T., Kondo, N., and Shirakawa, M. (2003) The structure and binding mode of interleukin-18. *Nat. Struct. Biol.* **10**, 966–971
57. Xiang, Y., and Moss, B. (2001) Determination of the functional epitopes of human interleukin-18-binding protein by site-directed mutagenesis. *J. Biol. Chem.* **276**, 17380–17386
58. Kim, S. H., Eisenstein, M., Reznikov, L., Fantuzzi, G., Novick, D., Rubinstein, M., and Dinarello, C. A. (2000) Structural requirements of six naturally occurring isoforms of the IL-18 binding protein to inhibit IL-18. *Proc. Natl. Acad. Sci. U. S. A.* **97**, 1190–1195
59. Kim, S. H., Azam, T., Novick, D., Yoon, D. Y., Reznikov, L. L., Bufler, P., Rubinstein, M., and Dinarello, C. A. (2002) Identification of amino acid residues critical for biological activity in human interleukin-18. *J. Biol. Chem.* **277**, 10998–11003
60. Gupta, A., Fei, Y. D., Kim, T. Y., Xie, A., Batai, K., Greener, I., Tang, H., Ciftci-Yilmaz, S., Juneman, E., Indik, J. H., Shi, G., Christensen, J., Gupta, G., Hillery, C., Kansal, M. M., *et al.* (2021) IL-18 mediates sickle cell cardiomyopathy and ventricular arrhythmias. *Blood* **137**, 1208–1218
61. Au, L., Fendler, A., Shepherd, S. T. C., Rzeniewicz, K., Cerrone, M., Byrne, F., Carlyle, E., Edmonds, K., Del Rosario, L., Shon, J., Haynes, W. A., Ward, B., Shum, B., Gordon, W., Gerard, C. L., *et al.* (2021) Cytokine release syndrome in a patient with colorectal cancer after vaccination with BNT162b2. *Nat. Med.* **27**, 1362–1366
62. Karki, R., Sharma, B. R., Tuladhar, S., Williams, E. P., Zalduondo, L., Samir, P., Zheng, M., Sundaram, B., Banoth, B., Malireddi, R. K. S., Schreiner, P., Neale, G., Vogel, P., Webby, R., Jonsson, C. B., *et al.* (2021) Synergism of TNF-α and IFN-γ triggers inflammatory cell death, tissue damage, and mortality in SARS-CoV-2 infection and cytokine shock syndromes. *Cell* **184**, 149–168.e17
63. Gisby, J., Clarke, C. L., Medjeral-Thomas, N., Malik, T. H., Papadaki, A., Mortimer, P. M., Buang, N. B., Lewis, S., Pereira, M., Toulza, F., Fagnano, E., Mawhin, M. A., Dutton, E. E., Tapeng, L., Richard, A. C., *et al.* (2021) Longitudinal proteomic profiling of dialysis patients with COVID-19 reveals markers of severity and predictors of death. *Elife* **10**, e64827
64. Vecchié, A., Bonaventura, A., Toldo, S., Dagna, L., Dinarello, C. A., and Abbate, A. (2021) IL-18 and infections: Is there a role for targeted therapies? *J. Cell Physiol.* **236**, 1638–1657
65. Jamilloux, Y., Henry, T., Belot, A., Viel, S., Fauter, M., El Jammal, T., Walzer, T., François, B., and Sève, P. (2020) Should we stimulate or suppress immune responses in COVID-19? Cytokine and anti-cytokine interventions. *Autoimmun. Rev.* **19**, 102567
66. Zhou, T., Damsky, W., Weizman, O. E., McGeary, M. K., Hartmann, K. P., Rosen, C. E., Fischer, S., Jackson, R., Flavell, R. A., Wang, J., Sanmamed, M. F., Bosenberg, M. W., and Ring, A. M. (2020) IL-18BP is a secreted immune checkpoint and barrier to IL-18 immunotherapy. *Nature* **583**, 609–614
67. Aricescu, A. R., Lu, W., and Jones, E. Y. (2006) A time- and cost-efficient system for high-level protein production in mammalian cells. *Acta Crystallogr. D Biol. Crystallogr.* **62**, 1243–1250
68. Reeves, P. J., Callewaert, N., Contreras, R., and Khorana, H. G. (2002) Structure and function in rhodopsin : High-level expression of rhodopsin with restricted and homogeneous N-glycosylation by a tetracycline-inducible N-acetylglucosaminyltransferase I-negative HEK293S stable mammalian cell line. *Proc. Natl. Acad. Sci. U. S. A.* **99**, 13419–13424
69. Scheuermann, T. H. (2015) High-precision, automated integration of multiple isothermal titration calorimetric thermograms: New features of NITPIC. *Methods* **76**, 87–98
70. Piszczek, G. (2015) SEDPHAT – a platform for global ITC analysis and global multi-method analysis of molecular interactions. *Methods* **76**, 137–148
71. Madeira, F., Park, Y. M., Lee, J., Buso, N., Gur, T., Madhusoodanan, N., Basutkar, P., Tivey, A. R. N., Potter, S. C., Finn, R. D., and Lopez, R. (2019) The EMBL-EBI search and sequence analysis tools APIs in 2019. *Nucleic Acids Res.* **47**, W636–W641

72. Guex, N., and Peitsch, M. C. (1997) SWISS-MODEL and the Swiss-Pdb Viewer: An environment for comparative protein modeling. *Electrophoresis* **18**, 2714–2723
73. R. Gupta, E. J., and Brunak, S. (2002) Prediction of glycosylation across the human proteome and the correlation to protein function. *Pac. Symp. Biocomput.*, 310–322
74. Steentoft, C., Vakhrushev, S. Y., Joshi, H. J., Kong, Y., Vester-Christensen, M. B., Schjoldager, K. T.-B. G., Lavrsen, K., Dabelsteen, S., Pedersen, N. B., Marcos-Silva, L., Gupta, R., Paul Bennett, E., Mandel, U., Brunak, S., Wandall, H. H., *et al.* (2013) Precision mapping of the human O-GalNAc glycoproteome through SimpleCell technology. *EMBO J.* **32**, 1478–1488
75. Dosztanyi, Z., Csizmok, V., Tompa, P., and Simon, I. (2005) IUPred: Web server for the prediction of intrinsically unstructured regions of proteins based on estimated energy content. *Bioinformatics* **21**, 3433–3434
76. Robert, X., and Gouet, P. (2014) Deciphering key features in protein structures with the new ENDscript server. *Nucleic Acids Res.* **42**, W320–W324
77. DeLano, W. L. (2015) *The PyMOL Molecular Graphics System, Version∼1.8*, Schrödinger, LLC, New York
78. Krissinel, E., and Henrick, K. (2007) Inference of macromolecular assemblies from crystalline state. *J. Mol. Biol.* **372**, 774–797
79. Kabsch, W., and IUCr. (2010) XDS. *Acta Crystallogr. D Biol. Crystallogr.* **66**, 125–132
80. McCoy, A. J., Grosse-Kunstleve, R. W., Adams, P. D., Winn, M. D., Storoni, L. C., and Read, R. J. (2007) Phaser crystallographic software. *J. Appl. Crystallogr.* **40**, 658–674
81. Emsley, P., Lohkamp, B., Scott, W. G., Cowtan, K., and IUCr. (2010) Features and development of coot. *Acta Crystallogr. D Biol. Crystallogr.* **66**, 486–501
82. Adams, P. D., Afonine, P. V., Bunkóczi, G., Chen, V. B., Davis, I. W., Echols, N., Headd, J. J., Hung, L.-W., Kapral, G. J., Grosse-Kunstleve, R. W., McCoy, A. J., Moriarty, N. W., Oeffner, R., Read, R. J., Richardson, D. C., *et al.* (2010) PHENIX: A comprehensive python-based system for macromolecular structure solution. *Acta Crystallogr. D Biol. Crystallogr.* **66**, 213–221
83. Esteban, D. J., and Buller, R. M. L. M. L. (2004) Identification of residues in an orthopoxvirus interleukin-18 binding protein involved in ligand binding and species specificity. *Virology* **323**, 197–207
84. Kim, S.-H. M., Azam, T., Yoon, D.-Y., Reznikov, L. L., Novick, D., Rubinstein, M., and Dinarello, C. A. (2002) Site-specific mutations in the mature form of human IL-18 with enhanced biological activity and decreased neutralization by IL-18 binding protein. *Proc. Natl. Acad. Sci. U. S. A.* **98**, 3304–3309
85. Ashkenazy, H., Abadi, S., Martz, E., Chay, O., Mayrose, I., Pupko, T., and Ben-Tal, N. (2016) ConSurf 2016: An improved methodology to estimate and visualize evolutionary conservation in macromolecules. *Nucleic Acids Res.* **44**, W344–W350